AFRL-VS-HA-TR-2007-1080

High-Resolution Seismic Velocity and Attenuation Structure of the Sichuan-Yunnan Region, Southwest China, Using Seismic Catalog and Waveform Data

Haijiang Zhang
Yunfeng Liu
Clifford H. Thurber
Zhen Xu
Xiaodong Song

University of Wisconsin
750 University Avenue
Madison, WI 53706-1490

Final Report

13 July 2007

AIR FORCE RESEARCH LABORATORY
Space Vehicles Directorate
29 Randolph Road
AIR FORCE MATERIEL COMMAND
Hanscom AFB, MA 01731-3010

NOTICES

Using Government drawings, specifications, or other data included in this document for any purpose other than Government procurement does not in any way obligate the U.S. Government. The fact that the Government formulated or supplied the drawings, specifications, or other data does not license the holder or any other person or corporation; or convey any rights or permission to manufacture, use, or sell any patented invention that may relate to them.

This report was cleared for public release and is available to the general public, including foreign nationals. Qualified requestors may obtain additional copies from the Defense Technical Information Center (DTIC) (http://www.dtic.mil). All others should apply to the National Technical Information Service.

AFRL-VS-HA-TR-2007-1080 HAS BEEN REVIEWED AND IS APPROVED FOR PUBLICATION IN ACCORDANCE WITH ASSIGNED DISTRIBUTION STATEMENT.

//Signature//	//Signature//
ROBERT J. RAISTRICK Contract Manager	BRIAN GRIFFITH, Maj, USAF, Chief Battlespace Surveillance Innovation Center

This report is published in the interest of scientific and technical information exchange, and its publication does not constitute the Government's approval or disapproval of its ideas or findings.

REPORT DOCUMENTATION PAGE

Form Approved
OMB No. 0704-0188

1. REPORT DATE *(DD-MM-YYYY)*	2. REPORT TYPE	3. DATES COVERED *(From - To)*
13-Jul-2007	Final Report	15-Apr-2006 to 15 Apr 2007

4. TITLE AND SUBTITLE
HIGH-RESOLUTION SEISMIC VELOCITY AND ATTENUATION STRUCTURE OF THE SICHUAN-YUNNAN REGION, SOUTHWEST CHINA, USING SEISMIC CATALOG AND WAVEFORM DATA

5a. CONTRACT NUMBER
FA8718-05-C-0016

5b. GRANT NUMBER

5c. PROGRAM ELEMENT NUMBER
62601F

6. AUTHOR(S)
Haijiang Zhang[1], Yunfeng Liu[1], Clifford H. Thurber[1], Zhen Xu[2] and Xiaodong Song[2]

5d. PROJECT NUMBER
1010

5e. TASK NUMBER
SM

5f. WORK UNIT NUMBER
A1

7. PERFORMING ORGANIZATION NAME(S) AND ADDRESS(ES)

University of Wisconsin
750 University Avenue
Madison, WI 53706-1490

8. PERFORMING ORGANIZATION REPORT NUMBER

9. SPONSORING / MONITORING AGENCY NAME(S) AND ADDRESS(ES)
Air Force Research Laboratory
29 Randolph Road
Hanscom AFB, MA 01731-3010

10. SPONSOR/MONITOR'S ACRONYM(S)
AFRL/VSBYE

11. SPONSOR/MONITOR'S REPORT NUMBER(S)
AFRL-VS-HA-TR-2007-1080

12. DISTRIBUTION / AVAILABILITY STATEMENT
Approved for Public Release; Distribution Unlimited.

[1]University of Wisconsin-Madison, [2]University of Illinois at Urbana-Champaign

13. SUPPLEMENTARY NOTES

14. ABSTRACT

The Sichuan-Yunnan region in southwestern China lies in the transition zone between the uplifted Tibetan plateau to the west and the Yangtze continental platform to the east. This region has a very complicated geological structure and is one of the most active areas of continental earthquakes in the world. This two-year project is to develop high-resolution models of the velocity and attenuation structure of the Sichuan-Yunnan region (longitudes ~97–108°E and latitudes ~21–35°N) using seismic catalog and waveform data.

There are four main components in this project: (1) using waveform alignment methods (waveform cross-correlation and bispectrum analysis) to obtain more accurate differential arrival times, (2) using regional scale adaptive-grid double-difference tomography to obtain detailed P- and S-wave velocity models of the Sichuan-Yunnan region, (3) using the adaptive-grid "triple-difference" seismic attenuation method to determine the detailed attenuation structure for both Qp and Qs for the Yunnan region, and (4) assembling a ground truth database.

15. SUBJECT TERMS
Seismic characterization, Seismic propagation

16. SECURITY CLASSIFICATION OF:			17. LIMITATION OF ABSTRACT	18. NUMBER OF PAGES	19a. NAME OF RESPONSIBLE PERSON
					Robert J. Raistrick
a. REPORT	b. ABSTRACT	c. THIS PAGE	SAR	62	19b. TELEPHONE NUMBER *(include area code)*
UNCLAS	UNCLAS	UNCLAS			781-377-3726

Standard Form 298 (Rev. 8-98)
Prescribed by ANSI Std. 239.18

Table of Contents

Figures

1. Introduction

One of the fundamental problems facing discrimination and location of earthquakes and explosions is creating accurate structure models for the crust and mantle. The routine practice of locating seismic events based on a one-dimensional velocity model inevitably introduces bias into locations. Using a high-resolution three-dimensional (3D) seismic velocity model significantly improves seismic event location accuracy (Smith and Ekstrom, 1996; Firbas, 2000; Steck et al., 2000) and thus helps to satisfy the goal of nuclear explosion monitoring. In addition to seismic event locations, seismic wave amplitudes are also important in discriminating between earthquakes and explosions. For example, the Lg/Pg ratio has been shown to be an effective discriminant (Jiao et al., 2003). As seismic waves travel through an anelastic and heterogeneous medium, their amplitudes will be attenuated and knowledge of the attenuation structure is vital to correct the distortion. Here we developed high-resolution models of the seismic velocity and attenuation structure of the Sichuan-Yunnan region (97^{o}–108^{o}E and 21^{o}–35^{o}N) that is located in southwest China using seismic catalog and waveform data.

The Sichuan-Yunnan region lies in an active transition zone between the Yangtze platform to the east and the Tibetan plateau to the west and is generally believed to have had its origin in the collision between the Indian plate and the Eurasian plate about 45 Ma ago. This continental collision led to active tectonic deformation on a larger-scale and created a high level of seismicity (Figure 1). There are seven major active seismic zones in this region including the Longmen Shan belt, the Xianshuihe seismic belt, the Anninghe seismic belt, the Xiaojiang seismic belt, the Red River seismic belt, the Lancang-Gengma seismic belt, and the Tengchong-Longling seismic belt (Chan et al., 2001). Most, but not all, of the earthquakes in these belts are associated with fault zones that are identified at the surface (Figure 1). Obtaining a high-resolution seismic velocity model for this region and precise earthquake locations will help delineate fault zones at depth more clearly and facilitate their association with surface fault traces. Several magnitude 7 earthquakes occurred in this region in the last twenty years. Recent examples are the 1995 Mengnian earthquake (M=7.4) and the 1996 Lijiang earthquake (M=7.0). The auxiliary IMS station KMI is located in this region and China's nuclear test site Lop Nor is located about 1000 km to the northwest.

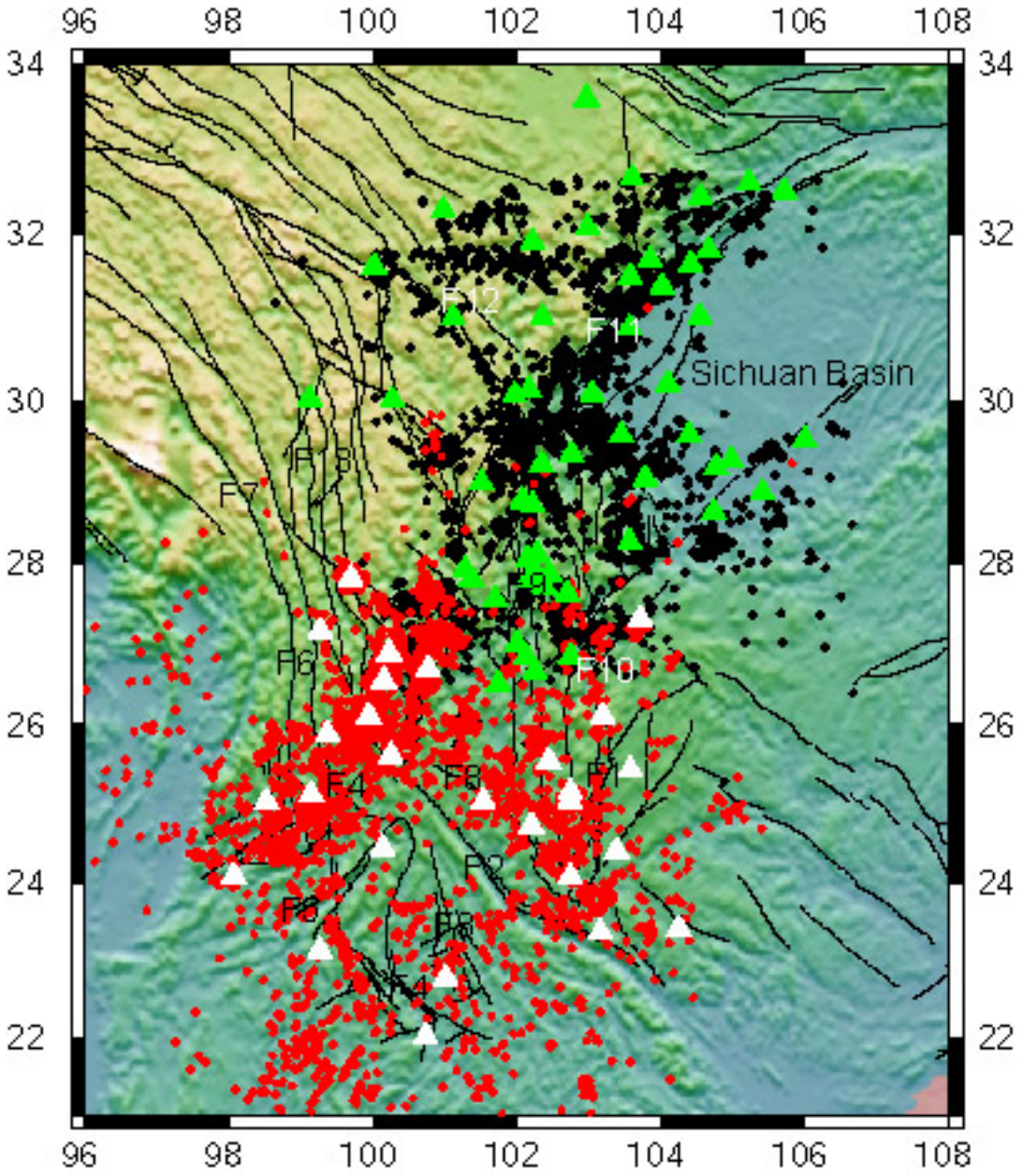

Figure 1. Relocated earthquakes in the Yunnan (red dots) and Sichuan (black dots) region from this study. White and green triangles are Yunnan and Sichuan provincial seismic stations. Black lines are mapped fault traces on the surface. F1: Xiaojiang Fault; F2: Red River Fault; F3: Wuliangshan Fault; F4: Lancangjiang Fault; F5: Nandinghe Fault; F6: Nujiang Fault; F7: Qiaohou-Weishan Fault; F8: Tonghai-Chuxiong Fault; F9: Anninghe Fault; F10: Zemuhe Fault; F11: Longmenshan Fault; F12: Xianshuihe Fault; F13: Jinshajiang Fault.

Most of the previous seismic tomography studies that cover the Sichuan-Yunnan region are on a global scale. Examples include the CUB 1.0 (Shapiro and Ritzwoller, 2002) and the Science Applications International Corporation (SAIC) global $1^o \times 1^o$ models that were constructed from group and phase velocity dispersion measurements of surface waves, and the CRUST 5.1 (Mooney, 1998) and CRUST 2.0 (Laske et al., 2001) models from seismic refraction data. There

are also some regional models in China such as the Pn model of Hearn and Ni (2001), the Pn and Sn velocity model of Ritzwoller et al. (2002), P-wave models of Liu et al. (1990), Xu et al. (2002), and Sun et al. (2004), and surface-wave models of Wu et al. (1997) and Lebedev and Nolet (2003). The grid spacing ranges from $1^o \times 1^o$ to $5^o \times 5^o$ and are too coarse to characterize the detailed structure of the Sichuan-Yunnan region. The most recent work by Huang et al. (2003) and Liang et al. (2004) used a smaller grid spacing of 0.5^o to calculate a Pn model for this region that shows the Pn velocity of uppermost mantle varies from 7.7～8.3 km/s. Regional 3D velocity models are also available for the Yunnan-Sichuan region from several studies (He et al., 2005; Huang et al., 2002; Liu et al., 2005; Wang et al., 2003). Huang et al. (2002) determined a 3-D Vp model for the Sichuan-Yunnan region (22^o–32^oN, 98^o–105^oE) with a horizontal grid spacing of 50 to 80 km and a vertical grid spacing of 10-25 km using 1315 local and regional earthquakes of magnitude > 2.5 and 172 stations. S times were only used to locate earthquakes. Wang et al. (2003) used P and S arrival times from 4625 local and regional earthquakes recorded at 174 stations to determine Vp and Vs models of southwestern China (21^o–34^oN, 97^o–105^oE). The grid spacing in horizontal directions is 0.5^o and the vertical spacing ranges from 10 km to 20 km. Different from Huang et al. (2002) and Wang et al. (2003), Liu et al. (2005) used arrival times from 602 local and regional earthquakes and 985 teleseismic events to determine a 3D Vp model beneath the north-south tectonic belt between Tibet and Eastern China. The grid spacing in the horizontal direction is 0.5^o and the vertical spacing is 20-35 km except for a finer grid interval of 3 km near the surface. In addition to 3D seismic tomography studies using body waves, He et al. (2005) used short-period (1-18 s) surface wave data recorded by 23 stations in the Yunnan region to determine a 3D S-wave velocity structure of the middle and upper crust.

Our recent development and applications of double-difference (DD) tomography showed that the new method has the ability to characterize the detailed velocity structure and improve seismic event locations in a superior manner compared to conventional seismic tomography (Zhang and Thurber, 2003, 2005, 2006; Zhang et al., 2004; Thurber et al., 2004). DD tomography is a generalization of DD location (Waldhauser and Ellsworth, 2000); it simultaneously solves for the 3D velocity structure and seismic event locations. DD tomography uses a combination of absolute and more accurate differential arrival times and hierarchically determines the velocity structure from larger scale to smaller scale. Recent application of DD location in this region (Yang et al., 2003; 2005) showed that the relocated events are more concentrated near the fault zones using just the catalog differential data. From their location results, we are confident that even using the catalog data alone will significantly improve the velocity model, though the best results will be achieved with waveform alignment methods.

To our knowledge, there has been no attenuation tomography study published for this region. There are some surface wave (Lg) and Pn wave attenuation studies in the Tibetan plateau that is located to the west of our targeted region (Xie et al., 2002; Xie, 2003). They found low Lg Q values (at 1 Hz) of typically lower than 200 in the entire plateau that are consistent with high temperature and/or fluids in the Tibetan crust (Xie et al., 2002). The frequency independent P wave Q values imply that a melt-bearing uppermost mantle might lie underneath Tibet (Xie, 2003).

Because of the high seismicity (more than 1000 earthquakes with magnitudes greater than 2.5 per year) and severe earthquake hazards, the Sichuan and Yunnan Seismological Bureaus have been operating dense local networks of stations since the 1970s (Figure 1). Most of the stations

were upgraded to short-period and broadband (up to 30 s) digital stations after 1999. We acquired P and S arrival times recorded by local network stations for the entire Sichuan-Yunnan region (Figure 1). We also acquired seismic waveforms for the Yunnan region in the period of 1999 to 2004. Using these catalog picks and waveforms, we determined 3D Vp and Vs models for the Yunnan-Sichuan region and 3D Qp and Qs models for the Yunnan region. Our research project consists of four components:

(1) using waveform alignment methods (waveform cross-correlation (WCC) and bispectrum (BS) analysis) to obtain more accurate differential arrival times for the Yunnan region;
(2) using regional scale adaptive-grid DD tomography to obtain detailed P- and S-wave velocity models of the Sichuan-Yunnan region;
(3) developing an adaptive-grid "triple-difference" seismic attenuation method and applying it to determine the detailed seismic attenuation structure for both Qp and Qs for the Yunnan region;
(4) assembling a ground truth database.

In the following sections, we will give a detailed description of each component including methods and results.

2. Data collection for the Yunnan-Sichuan region

Yunnan region. We collected 3-component waveforms recorded by 26 Yunnan provincial stations for ~5000 events in the period of 1999 to 2004. It was time consuming and laborious to process these waveforms to be used for WCC analysis. First we converted all the waveforms stored in the original China data format into standard SAC format required by the BCSEIS package (Du et al., 2004). Then we matched these waveforms with the catalog picks we already collected and filled the corresponding SAC headers. For the waveforms that did not have matched catalog picks, we first used the wavelet-AIC picker (Zhang et al., 2003) to automatically pick first P and S arrivals. The picker was originally designed to only pick first P arrivals. We adapted it to pick first S arrivals on horizontal components. We first calculated the first S arrivals based on the catalog locations and an approximate 3D Vs model. Then we started the time window for the wavelet-AIC picker 5 seconds before the estimated S arrivals and compared the picks selected for the two horizontal components. If the two selected picks are reasonably close to each other (e.g. within ~1 second), then we chose the mean of the two picks as the first S arrivals. For quality control, we visually checked all the waveforms and corrected and removed those outliers. In this way, we can guarantee the quality of P and S picks. After this process, we obtained ~35000 P and ~30000 S picks for ~5600 events recorded by 26 stations (Figure 1).

Sichuan region. We assembled and analyzed catalog picks for various local networks in the Sichuan region. In total, there are ~ 41400 P and ~38700 S picks corresponding to ~5000 earthquakes and ~50 stations (Figure 1). Compared to the Yunnan region, there were not many waveforms available. We first analyzed a total of 2651 high-quality waveforms for 267 events at 16 stations. We further analyzed an additional ~80 events that do not have catalog locations and origin times. We estimated initial locations and origin times for these events using a grid search method NonLinLoc developed by Anthony Lomax. The absolute P and S arrivals extracted from these waveforms along with other catalog picks are used for seismic tomography.

3. Waveform cross-correlation using the bispectrum (BS) method, BCSEIS

Researchers using cross-correlation (CC) to align waveforms often choose those time delay estimates with CC coefficients above a specified threshold. For example, Schaff et al., (2002) only select those time delays with CC values larger than 0.70 and mean coherences above 0.70. The selection of an optimum threshold value for waveform cross-correlation is important but difficult. If it is set too high, then only a limited number of very accurate differential time data are available for further analysis. If the threshold value is set too low, then many unreliable differential time estimates are used which will negatively affect the relocation and tomography results.

The BCSEIS algorithm that we adopted for measuring waveform CC times works in the third-order spectral domain and can suppress correlated Gaussian or low-skewness noise sources (Nikias and Raghuveer, 1987; Nikias and Pan, 1988). BCSEIS employs a third-order spectral method to calculate two additional time delay estimates with both the raw (unfiltered) and band-pass filtered waveforms, and uses them to verify (select or reject) the one computed with the CC technique using the filtered waveforms (Du et al., 2004). Thus this BS verification process can reject unreliable CC time delay estimates and also can accept additional CC time delays even if their associated CC coefficients are smaller than a nominal threshold value if they pass the BS verification procedure (Du et al., 2004).

We have calculated differential times for ~38000 waveforms for ~5600 events recorded by 26 stations in Yunnan Province using BCSEIS and obtained ~130000 P- and ~33000 S-wave differential travel times given estimated origin times. Figure 2 shows the distribution of the calculated P- and S-wave differential times. From the figure we can see that the majority of differential times are less than 1 second. Such measurements are associated with the event pairs with a separation of a few kilometers. The other measurements with larger differential times correspond to those event pairs that could be separated by more than 50 km and can also have similar P and S waveforms. We found that the calculated differential times with different filtering are slightly different for some waveform pairs. To assure that the results are not affected by filtering, we tested several different filters. We found that the default Butterworth filter with 3 poles and 2 passes in BCSEIS changes the waveform shape around the first arrivals significantly. After testing different filtering, we decided to choose a Butterworth filter with 2 poles and 1 pass in our correlation computation. We also tested different window sizes to find a suitable one for our analysis.

Figures 3 and 4 show the improvement of CC differential times over catalog picks for those similar events. In Figure 3, a set of similar waveforms observed at the station BST are aligned with the catalog P arrivals and CC differential times, separately. The stacked waveforms are shown in the bottom panels. Note that the waveforms are aligned relatively well using catalog picks, verifying the quality of the catalog picks (Figure 3). For comparison, we can see that the quality of the CC alignment is much better than that of the catalog pick alignment. As shown in the figures by vertical lines, the time window we choose here is 30 samples before and 97 samples after the preliminary P arrival picks. Similarly, Figure 4 shows waveform alignments with catalog S arrivals and CC differential times for another set of similar waveforms recorded at the station HQT. Due to the greater scattering (errors) in S arrival picking, the improvement of the CC alignment for S phases is even more significant. Similarly, we also obtained a total of ~4100 P and S differential times from 323 events recorded by 17 stations in the Sichuan region.

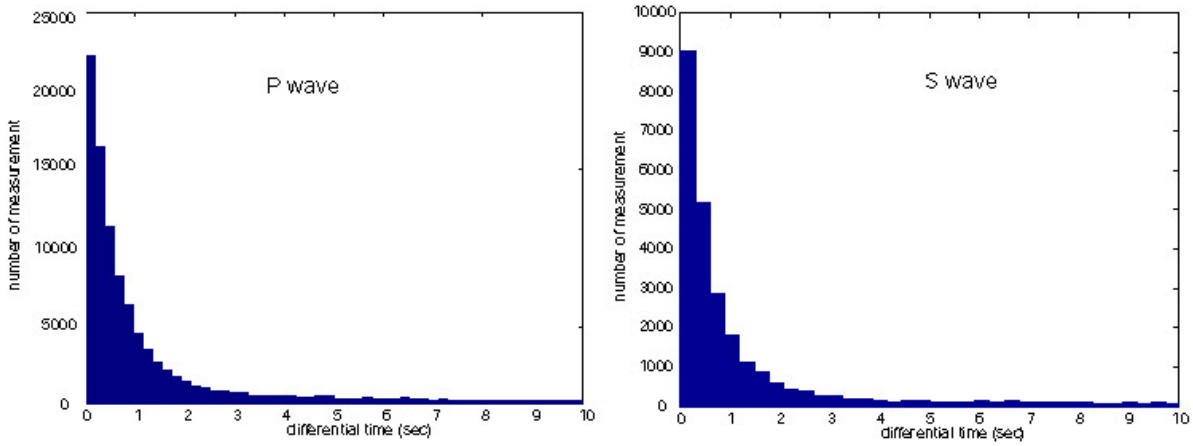

Figure 2. Distribution of the calculated P- and S-wave differential times using the waveform cross-correlation package BCSEIS for the Yunnan region.

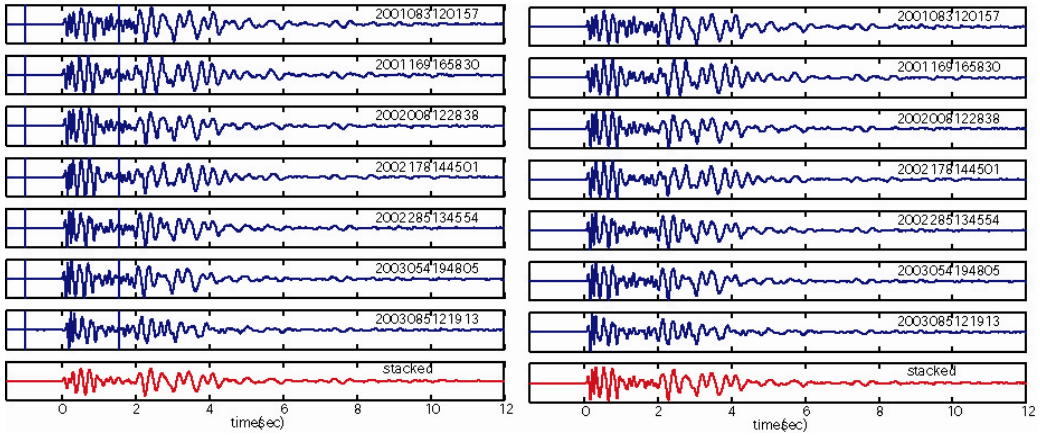

Figure 3. Waveform alignment according to (left) catalog P picks and (right) waveform cross-correlation P times.

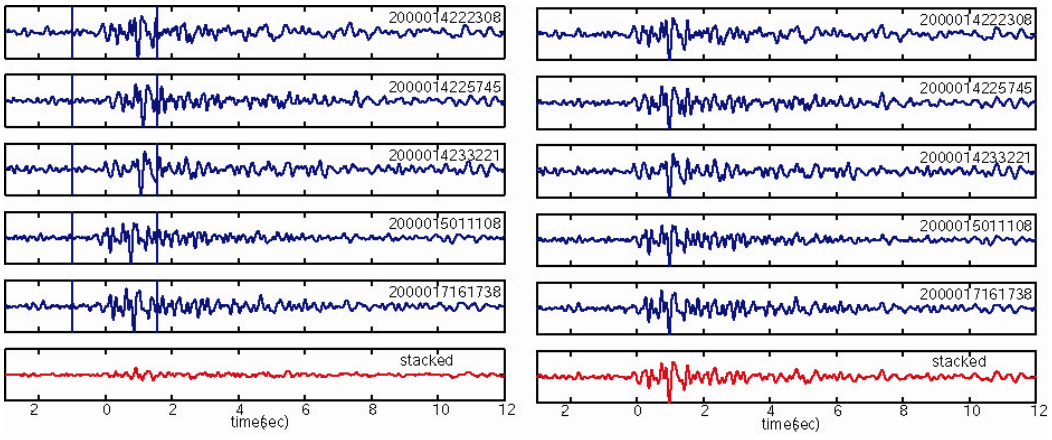

Figure 4. Waveform alignment according to (left) catalog S picks and (right) waveform cross-correlation S times.

4. Regional-scale adaptive-grid double-difference tomography method

Adaptive tomography method based on tetrahedral diagrams

The two most commonly used schemes to represent the Earth in seismic tomography are the regular constant-velocity cell approach (Aki and Lee, 1976) and the regular 3D grid approach (Thurber, 1983). The advantage of the regular constant-velocity cell approach is its simplicity, but because the velocity is constant inside a cell and discontinuous from one cell to another, cells are not ideal for approximating a smoothly varying structure, and finding accurate ray paths connecting events and stations can be difficult. For the regular 3D grid approach, the velocity varies continuously among nodes in all directions using linear B-spline interpolation (Thurber, 1983) or cubic B-spline interpolation (Michelini and McEvilly, 1991). No matter which approach is taken, however, the ray distribution typically is highly uneven due to inadequate acquisition geometry, uneven distribution of seismic sources, missing data, and ray bending. Some grid points or cells may have few or even no rays sampling them, while other cells may have very dense rays sampling them. The regular grid or cell spacing restriction makes it difficult to adapt the model to the uneven distribution of ray paths. The mismatch between the ray distribution and the grid or cells used results in instability of the inversion.

The goal of matching the ray distribution and the inversion grid or cells in seismic tomography naturally leads to the irregular grid or cells distribution. Sambridge and Gudmundsson (1998) and Bohm et al. (2000) proposed irregular cell approaches on the basis of tetrahedral and Voronoi diagrams, respectively. In the former study, they did not explicitly explain how to optimize the grid. In the latter study, the cells are adjusted based on the model null space energy (Vesnaver, 1996) and/or velocity gradient. For whole Earth tomography, Sambridge and Faletic (2003) recently proposed a data-driven tetrahedral cell adaptive scheme based on the maximum spatial gradients in seismic velocity perturbation across each tetrahedron face. The tetrahedral/Voronoi diagram methods allow a more flexible representation of the model. For example, cells of widely varying sizes with complex distributions are easily implemented, and it is more convenient to build parameterizations containing particular interfaces, on which the nodes can be distributed.

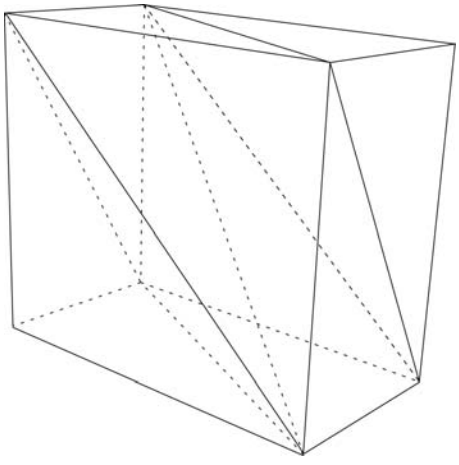

Figure 5. Tetrahedral diagram for a set of 8 nodes, defining a total of 6 tetrahedra.

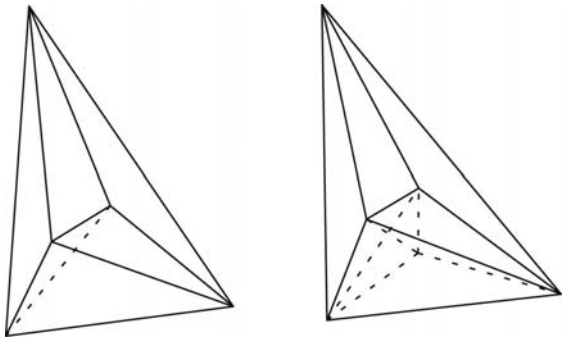

Figure 6. Set of tetrahedral before (left) and after (right) adding a node. Only the tetrahedron within which the new node is inserted is affected by the process.

We adopt the tetrahedral parameterization approach and associated interpolation schemes for our adaptive-grid DD tomography algorithm. Ideally, the distribution of the inversion grid should match with the data distribution: in regions where there are more rays, the inversion grid nodes should be more finely distributed. The inversion problem will then be better conditioned. Here we use the derivative weight sum (DWS) values at the grid nodes to indicate the ray density (Thurber, 1983). We start the inversion from a regular inversion grid, equivalent to that of the simul2000 algorithm (Thurber and Eberhart-Phillips, 1999). We randomly perturb the starting regular inversion grid by a very small amount (so that the nodes are not located on the same plane) in order to construct the tetrahedral or Voronoi diagram around these nodes using the Qhull algorithm (Barber *et al.*, 1996). Figure 5 shows the tetrahedral diagram for 8 starting regular nodes. We also construct a regular computational grid that remains fixed during the inversion, which can be the same as the starting regular inversion grid or finer, following the strategy of Kissling et al. (2001). On a local scale, we trace rays between events and stations based on the current regular velocity grid using a Cartesian pseudo-bending method (Um and Thurber, 1987). The rays between all the event and station pairs are saved for later use in defining the adaptive grid. Using these rays, we find the partial derivatives of the travel times with respect to the model slowness parameters on the initial (slightly irregular) inversion grid. In the process, we calculate the DWS values on the inversion grid nodes. We then automatically go through each tetrahedron to check the sum of the DWS values at its 4 nodes. If the sum is larger than a predefined threshold *threshold1*, an additional node will be inserted at the center of this tetrahedron. The velocity value at this node is interpolated by the linear interpolation method from the 4 inversion grid nodes or by the natural neighbor interpolation method from its N natural neighbors (Sambridge et al., 1995), depending on which interpolation method has been adopted. Figure 6 shows three tetrahedra constructed from 5 nodes. One additional node is inserted into the middle of the bottom tetrahedron creating 4 new tetrahedra (Figure 6). The advantage of refining one tetrahedron by adding a node inside it is to avoid affecting other neighboring tetrahedra. At the same time, we also remove all the inversion grid nodes having a DWS value smaller than the threshold *threshold2*. Generally *threshold1* is 30 times larger than *threshold2*. Note that we keep all the irregular grid nodes that were originally the boundary grid nodes of the starting regular inversion grid to guarantee all the regular computational grid nodes are located inside the tetrahedral or Voronoi diagram.

After this refining process, we obtain a new irregular inversion grid. This irregular inversion grid cannot be guaranteed to be data-adaptive without further quality control. We construct a revised tetrahedral or Voronoi diagram around the new irregular inversion grid and recalculate the DWS values on all the nodes using the previously saved ray information. After this, we examine all the irregular nodes to check if the DWS value on each one is greater than the predefined value *threshold2*. The irregular grid nodes not satisfying the requirement will be removed. This new irregular grid is the inversion grid to be used for the current iteration of simultaneous inversion. Finally a new tetrahedral diagram is constructed and the partial derivatives of the travel times with respect to the new set of inversion grid nodes are determined for the construction of the seismic tomography equations. After each simultaneous inversion, the velocity values on the irregular inversion grid nodes and the regular computational grid nodes are updated. For subsequent simultaneous inversions, the inversion grid is again adaptively updated to better match with the data distribution, following the same procedure.

"Sphere-in-a-box" finite-difference method

In the "sphere-in-a-box" version of DD tomography, the curvature of the Earth is explicitly taken into account. We note that the earth flattening transformation approach is only valid for 1D velocity models and not for 3D velocity models so that approach is not a viable one. Following Flanagan et al. (2007), we solve this problem by parameterizing a spherical surface inside a Cartesian volume of grid nodes. Figure 7a shows the case of putting the entire Earth into a cube so the curvature of the Earth can be taken into account. This scheme can be used for global seismic tomography. For regional seismic tomography, we are only interested in a part of the Earth and we can construct a rectangular box covering the portion of interest (Figure 7b and c). The coordinate center is placed at the surface of the Earth, positive X and Y-axes point to the direction of North and West, and positive Z-axis points downward. The grid nodes above the Earth's surface (air nodes) are given the velocity for P waves traveling in air (Figure 7c). As a result, all the rays travel inside the Earth. Here we should emphasize that this version is still based on a Cartesian coordinate system and not on a true spherical system.

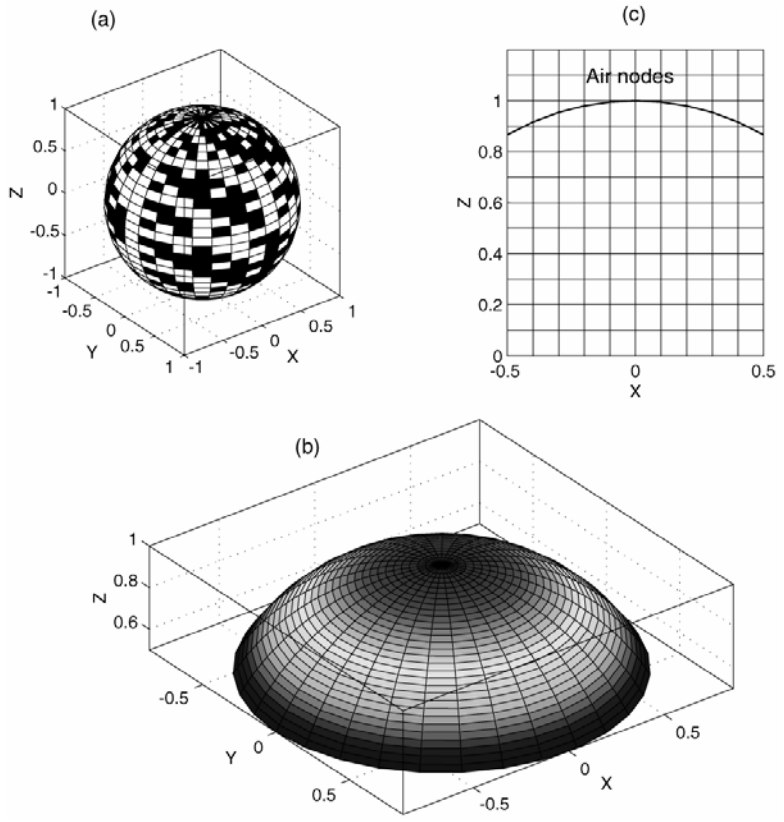

<u>Figure 7.</u> Grid setup for regional scale double-difference tomography. (a) The whole earth is inserted into a cubic box. (b) A rectangular box covers the region of interest. (c) The representation of (b) in the X-Z plane. The surface of the Earth is shown as a thick line. The regular grid is used for finite-difference ray tracing algorithm.

Finite-difference ray tracing algorithms require a uniformly spaced velocity (or slowness) grid (Podvin and Lecomte, 1991). We interpolate the velocity values on the regular uniform grid nodes from non-uniform inversion grid nodes through trilinear interpolation. First we treat each station as a source and calculate travel times to all velocity nodes in the volume. The travel time from a station to each earthquake is interpolated from its 8 neighboring nodes through trilinear interpolation. The ray path from the earthquake to the station is found iteratively with increments

opposite to the travel time gradient. The corresponding partial derivatives of travel times with respect to the slowness models are calculated by dividing the ray paths into small segments (Thurber, 1983).

Key modifications of the tomography code

During the project, we made several key modifications to make the code applicable to large data set on regional scales. First we modified the adaptive-mesh tomography code from local scale to regional scale by including the "sphere-in-a-box" finite-difference travel time calculation method. Previously the code had difficulty saving ray path information to adapt the inversion mesh due to the limitation of memory space (Zhang and Thurber, 2005). We overcame this challenge by modifying the code to save ray density information on an intermediate grid and then project it back to the adaptive inversion mesh.

We also modified the code by finding a way to apply the smoothing constraint to the inversion mesh. Previously, we set up an intermediate regular grid and then projected the smoothing weights on it to the inversion mesh (Zhang and Thurber, 2005). This could deteriorate the advantage of using an adaptive mesh to resolve the fine scale structure because the spatial scale of the structure is limited by the size of the intermediate grid. We now have found a way to efficiently search the natural neighbors for each inversion mesh node and are able to directly apply the first-order smoothing constraint.

The adaptive-mesh DD tomography code is further modified by also adding new nodes at the midpoints of tetrahedral edges when a tetrahedron is sampled by many rays, as determined by a threshold level. The previous strategy was to only add new nodes to the center of one tetrahedron. The new strategy will be helpful for more uniformly distributing the inversion mesh nodes.

5. Seismic attenuation tomography

Seismic attenuation can provide relatively independent and complementary information on subsurface structure (Sanders, 1993; Eberhart-Phillips et al., 1995; Romero et al., 1997). Examples of attenuation tomography applied to fault zone settings can be found in Lees and Lindley (1994), for Loma Prieta, and Rietbrock (2001), for Kobe.

Our approach will follow that of Rietbrock (2001). Briefly, the set of spectra for a given event at each of the observing stations j was fit to an Ω-square source model with a single corner frequency, using

$$\ln(A_j(f)) = \ln(\Omega_{0j}) - \ln(1 + (f/f_c)^2) - \pi\, f\, t_j^* \qquad (1)$$

where A_j is the spectral amplitude at frequency f for the event observed at station j, Ω_{0j} is the long-period spectral plateau level, f_c is the corner frequency for the event, and t_j^* is the whole path attenuation operator for the event path to station j (Rietbrock, 2001):

$$t_{ij}^* = \int_{path} \frac{dr}{V_{ij}(r)\, Q_{ij}(r)} \qquad (2)$$

Equation (1) is fit for the range of frequencies with adequate signal-to-noise ratio. The set of all t* values is then inverted for the 3D Q structure, using the 3D seismic velocity model and associated event locations to determine the ray paths for the t* integral. In fact, once the event locations and the 3D velocity model are determined, the relationship between the t* values and the reciprocal of the Q structure (1/Q) is linear.

Spectral-ratios between P and S arrivals at one station or between P arrivals at two stations for a single event have been used to derive differential t* values that are then inverted for relative Q variations (Roth and Wiens, 1999). This is essentially a "double-difference" attenuation tomography method (difference between observed and calculated differences in t*), which removes some of the systematic components from the equation. This can be taken one step further to produce a "triple-difference" attenuation tomography method, similar to the approach of Blakeslee et al. (1989). Expressing the amplitude spectrum from source i to station m as

$$A_{im}(f) = A_i(f,\theta_{im},\phi_{im})\, I_m(f)\, G_{im}(r) \exp(-f\pi t^*_{im}) \tag{3}$$

where A_i is the radiated source spectrum, I_m is the instrument response, and G_{im} is the geometric spreading, then for a pair of nearby events i and j observed at a pair of nearby stations l and m, we form the ratio of ratios

$$\frac{A_{il}(f)/A_{im}(f)}{A_{jl}(f)/A_{jm}(f)} = C(r)\,\frac{\exp(-\pi f(t^*_{il}+t^*_{jm}))}{\exp(-\pi f(t^*_{im}+t^*_{jl}))} \tag{4}$$

where C(r) is a ratio of ratios of the geometrical spreading terms (assumed to be independent of frequency), with the instrument responses and source spectral amplitudes canceling out (assuming that the radiated source spectra from a given event at two nearby stations are approximately equal). Taking the natural log, we arrive at

$$\ln\left(\frac{A_{il}(f)/A_{im}(f)}{A_{jl}(f)/A_{jm}(f)}\right) = \ln C(r) + f\pi\left((t^*_{jl}-t^*_{il})-(t^*_{jm}-t^*_{im})\right) \tag{5}$$

which is a linear function of frequency and can be fit to determine the observed t* difference term. Then the difference between the observed and calculated t* difference terms can be related to perturbations to the Q model via

$$\left[(t^*_{jl}-t^*_{il})-(t^*_{jm}-t^*_{im})\right]^{obs} - \left[(t^*_{jl}-t^*_{il})-(t^*_{jm}-t^*_{im})\right]^{cal} = \int\frac{dr}{V_{jl}\,\Delta Q_{jl}} - \int\frac{dr}{V_{il}\,\Delta Q_{il}} - \left[\int\frac{dr}{V_{jm}\,\Delta Q_{jm}} - \int\frac{dr}{V_{im}\,\Delta Q_{im}}\right] \tag{6}$$

The left-hand side can be thought of as a "triple difference." In principle, the difference data will be more accurate, and we can combine t* residuals, differential t* residuals (i.e. site-response corrected), and "triple difference" data to derive a more accurate Q model in a manner analogous to DD seismic velocity tomography (discussed above). We developed this refined attenuation modeling approach as part of this project. The adaptive-grid approach proposed in the above section is also adapted in the attenuation tomography in the same way as we do for the seismic tomography.

Measurement of the absolute t Values*

We fit spectral amplitude data to equation (1) within the range of frequencies with adequate signal-to-noise ratio to calculate t* values. We use the multitaper method of spectral analysis (Park et al., 1987) to calculate amplitude spectra from the windowed vertical waveforms around the P arrivals. We also estimate the noise spectra from the seismograms in a window right before the signal window.

In the traditional single-taper analysis, portions of the waveforms of interest are excluded from analysis as a trade-off for reducing the spectral leakage. In the multitaper approach, a family of statistically independent spectral estimates is computed from a signal using a set of orthogonal tapers that are referred to as discrete prolate spheriodal sequences (DPSS). Averaging over this ensemble of spectra yields an estimate with much lower variance than that from single-taper methods. Stable spectral estimation is of importance for a robust measurement of t* values.

Figure 8 shows samples of seismograms recorded at two stations HQT and EYA for two events with magnitude 3.3 and 4.0, respectively. The signal windows used for amplitude spectrum calculations are indicated by vertical lines in the figure. The corresponding multitaper spectra estimated from these seismograms are shown in Figure 9. In each panel of the figure, the calculated amplitude spectra are shown as solid lines, while the noise spectra are represented by dotted lines. The fits of spectral amplitude data to equation (1) are demonstrated with dashed lines. We obtain a set of Ω, f_c and t* values from the fits as shown in each panel of the figure (Figure 9). Using this method, we calculated ~10200 P-wave t* values from ~3000 events and ~8860 S-wave t* values from ~2300 events in the Yunnan region.

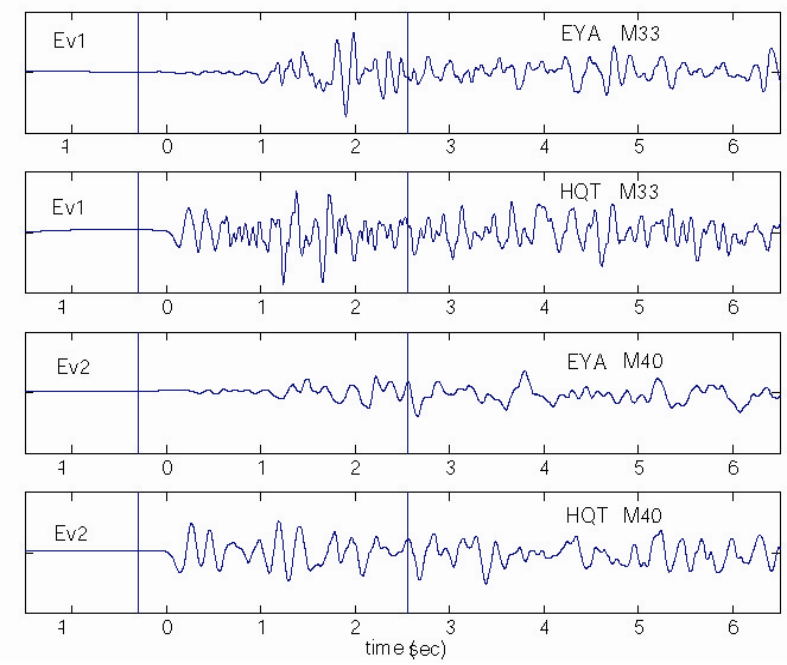

Figure 8. Waveforms at two nearby stations EYA and HQT from two nearby events.

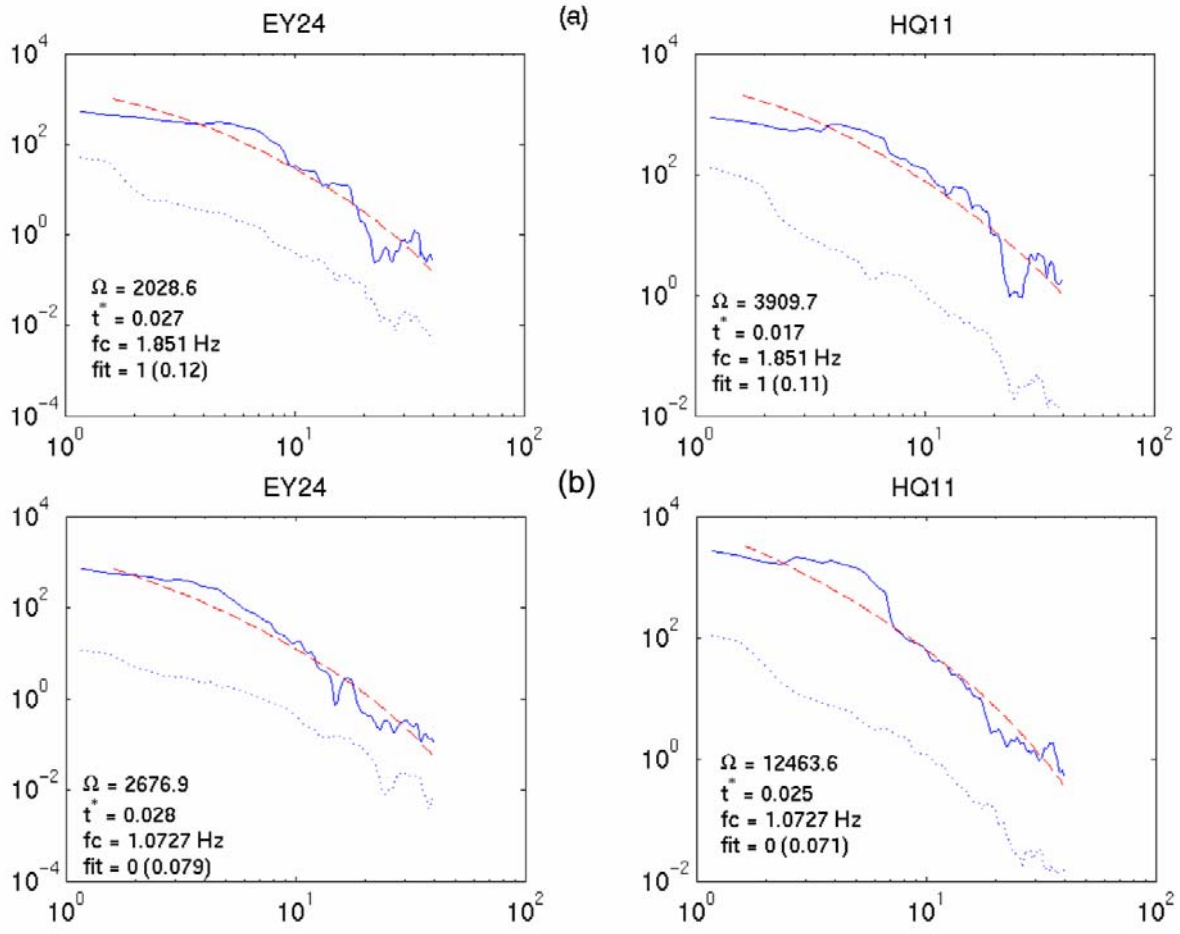

Figure 9. Spectral fitting based on Equation 1 to estimate t* values. Blue solid line: original spectra. Red dashed line: fitting spectra. Blue dots: noise spectra.

Measurement of differential t values using two events and two stations*

The above approach for measuring absolute t* values may potentially suffer limitations when there is significant site response at some stations. We have proposed to use two events and two stations to remove source signature and site response from the spectral amplitude using equations (4) and (5).

Figure 10 shows the calculated spectral ratios from the above two stations and two events. We fit spectral ratios to the linear equation (5) and get the differential t* value of 0.0066. The differential t* value calculated directly from the measured absolute t* values is 0.0070. These two values are close; however, the measured differential t* values from spectral ratios are free from station effects and are not affected by the source model assumption. These differential t* values can be used to solve for the Q model in a way similar to DD tomography. We note that the multitaper method also improves the robustness of spectral ratios significantly.

As can be seen in Figure 10, the estimated differential t* values may be affected significantly by the fitting frequency range. We developed an automatic process to calculate the estimated differential t* values in which the fitting frequency range is chosen based on signal-to-noise ratio (SNR) and fitting error. The optimal frequency range is selected when the SNR is larger than 3 and the standard deviation of the fitting line to the spectra is smallest. We measured ~120,000 differential t* values for P waves using this automatic process for ~1550 events on 23 stations of the Yunnan seismic network. Figure 11 shows the comparison of differential P-wave t* measurements with respect to those calculated directly using the Ω-square source model. It indicates that when the frequency range is larger, the discrepancy is smaller. For example, for the fitting frequency range greater than 37 Hz, there is a clear linear trend between the two measurements, indicating both absolute and differential t* measurements are reliable. Using the same procedure, we also calculated ~122,500 differential S-wave t* values for 1455 events on 24 stations. We compared these differential S-wave t* values to those calculated directly from the absolute t* values using the Ω-square source model. A similar conclusion to that for P waves can also be drawn.

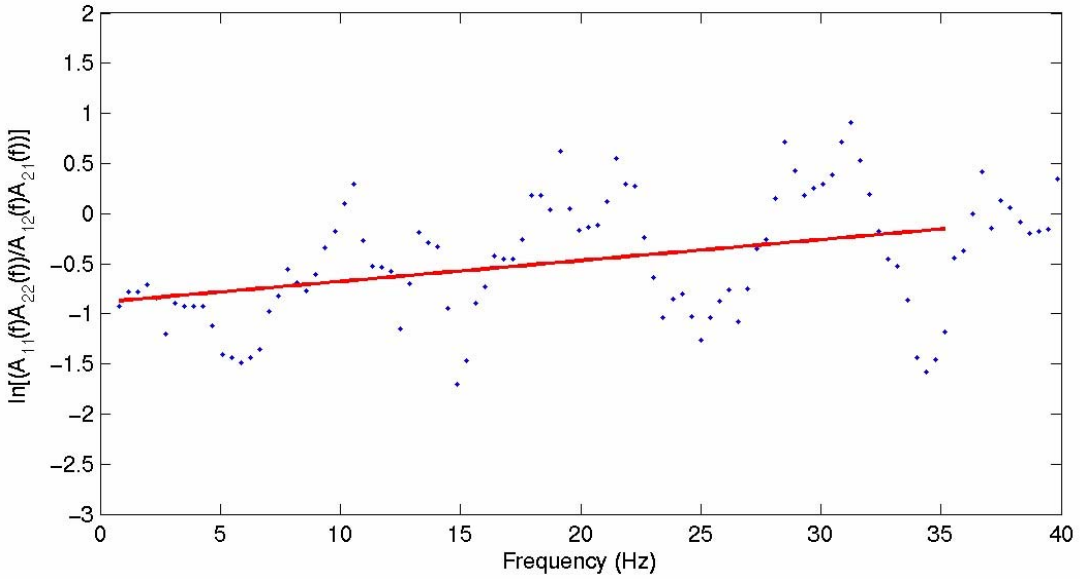

Figure 10. Differential t* measurements using spectral ratios for two events and two stations shown in Figure 9.

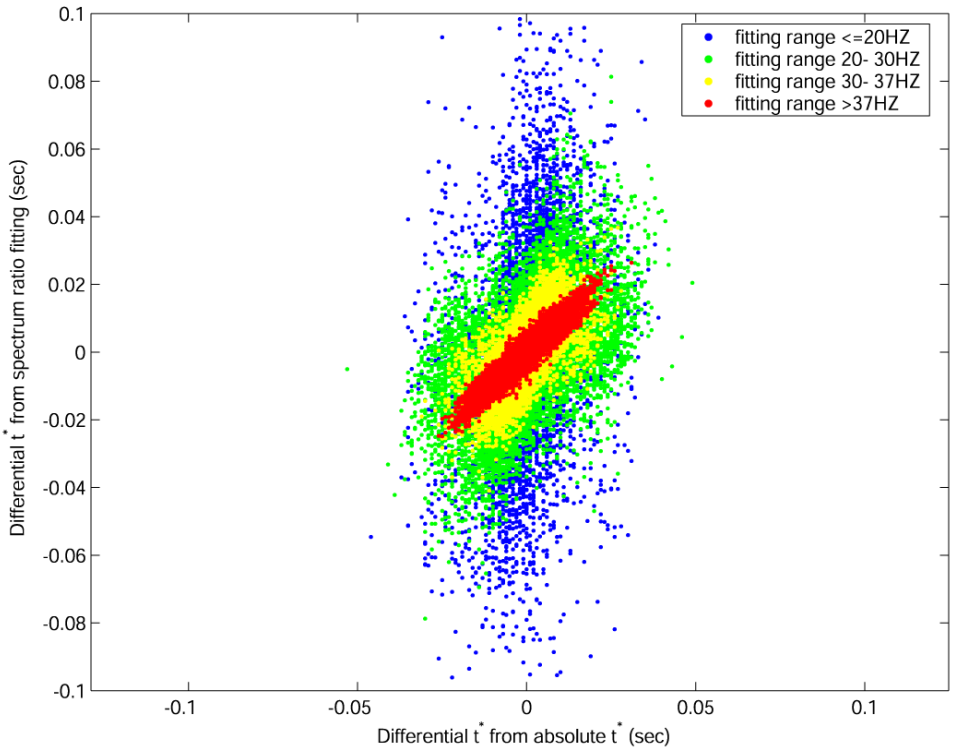

Figure 11. Comparison of measured differential t* values and those calculated directly from absolute t* values for P waves.

6. Earthquake locations and 3D velocity models in the Yunnan region

For the Yunnan region, we obtained ~96000 first P arrivals and ~32000 first S arrivals for ~5600 events and 26 stations (Figure 12). From them, we constructed ~289000 P and ~254000 S differential times for event pairs within 40 km. A maximum of 20 neighbors is allowed when forming links among event pairs. The average number of links (or common observations) per event pair is 8 and the average inter-event distance is 11 km. Along with ~96000 P and ~32000 S cross-correlation times, we used the double-difference tomography method to simultaneously determine earthquake locations and the Vp and Vs models.

We took a multi-step strategy to update event locations and the velocity models. First we started from a regular inversion grid in latitude, longitude and depth and an estimate 1D model. The grid spacing in latitude and longitude is 0.5^{o} and it is 5 km in depth from 0 km to 80 km. The initial RMS residuals for catalog times and CC times are 3.059 s and 5.471 s, respectively. We adopted a hierarchical weighting system for different data types (Zhang and Thurber, 2003, 2006). We first applied 10 times higher weighting to the absolute times to image the larger scale structure and move earthquakes closer to their locations. Then we applied higher weighting to the differential times (including catalog differential and CC times) to further refine the structure near the source region and improve earthquake locations. The final absolute and weighted RMS residuals for catalog times are 569 ms and 356 ms. For comparison, the final absolute and weighted RMS residuals for CC times are 69 ms and 39 ms. Both smoothing (weight=30) and damping are applied to stabilize the inversion. A grid interval of 5 km is used for finite-difference travel time calculation.

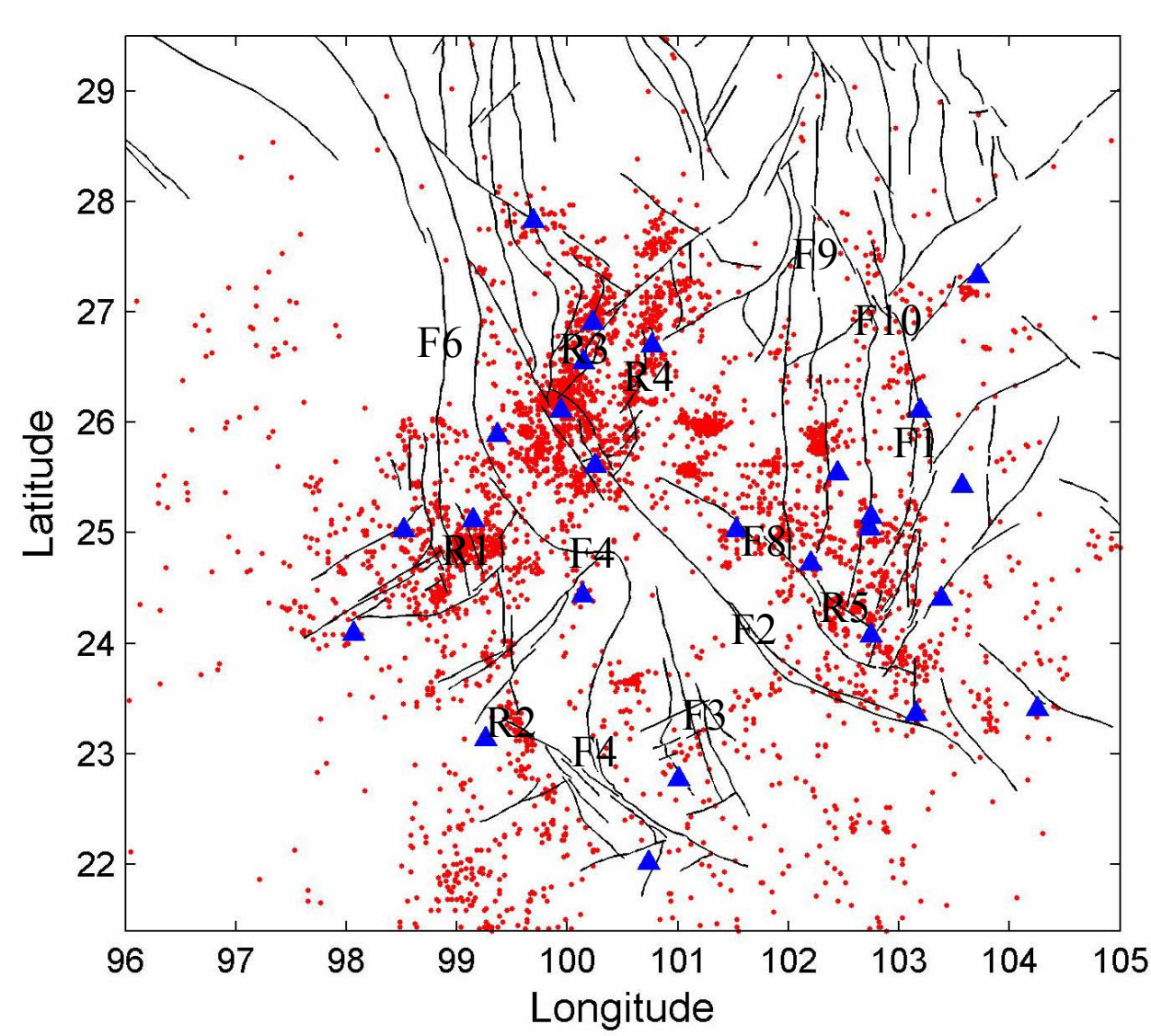

Figure 12. Event and station distribution for the Yunnan region. F1: Xiaojiang Fault; F2: Red River Fault; F3: Wuliangshan Fault; F4: Lancangjiang Fault; F5: Nandinghe Fault; F6: Nujiang Fault; F7: Qiaohou-Weishan Fault; F8: Tonghai-Chuxiong Fault; F9: Anninghe Fault; F10: Zemuhe Fault; R1: Tengchong-Longling seismic belt; R2: Lancang-Gengma seismic belt; R3: Lijiang seismic belt; R4: Yongshen-Ninglang-Muli-Juilong seismic belt; and R5: Tonghai-Shiping seismic belt.

We then started from the earthquake locations and velocity models inverted from the previous step and used only the more accurate CC times to further update the velocity models using the adaptive grid approach. Figure 13 shows the grid nodes at depths of 7.5 to 12.5 km after the inversion. It is clear to see that the density of grid nodes follows the earthquake distribution pattern shown in Figure 12. The final absolute and weighted RMS residuals for the CC times are 6 ms and 4 ms. The Vp and Vs models are stored on a grid that has a horizontal grid spacing of 0.2^{o} in latitude and longitude and a vertical grid spacing of 5 km in depth.

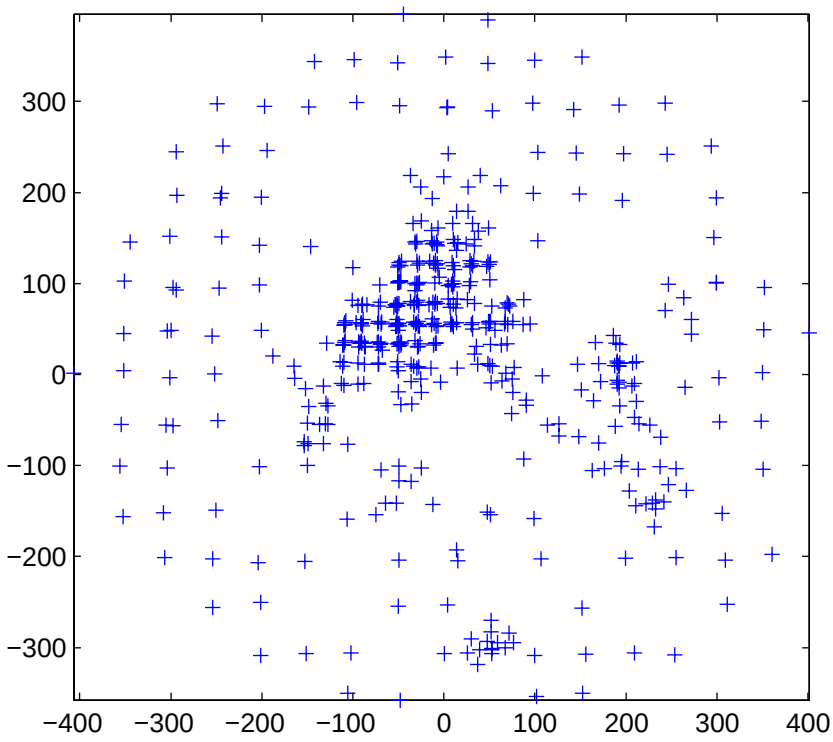

Figure 13. Inversion grid nodes for P wave at depths 7.5 km to 12.5 km for the adaptive-grid tomography.

Earthquake locations

The seismotectonic structures and seismicity in the Yunnan region are controlled by the collision between the Indian and Eurasia plates. As shown in Figure 12, there are a number of active faults in the region. The major active faults include the Red River Fault (F2), the Xiaojiang Faut (F1), and the Qiaohou-Weishan Fault (F7). The slip rate on the Red River fault is as large as about 7 – 9 mm/year on the southern segment of the fault (Su and Qin, 2001). Several large earthquakes (e.g. the 1925 M 7 Dali earthquake) have occurred along the Red River Fault. Along the Xiaojiang Faut, the slip rate is about 6.4 – 8.8 mm/year (Li, 1993; Su and Qin, 2001). The strong earthquakes associated with the fault include the 1833 M8 Songming earthquake and the 1966 M6.5 Dongchuan earthquake. These two faults along with the Xianshuihe Fault and Jinshajiang Fault (in the north of the region) form a seismically-active zone, which surrounds a rhomboid-like block, known as the Sichuan-Yunnan block. In addition to this seismically-active zone, there are several other active areas in the region. Two large earthquakes with Ms 7.3 and Ms 7.4 occurred in the Tengchong-Longling seismic belt (R1) on May 29, 1976 only about 100 minutes apart. Similarly, another pair of earthquakes of Ms 7.4 and Ms 7.2 took place within about 12 minutes along the Lancang-Gengma seismic belt (R2) on November 6, 1988. An M 7.0 earthquake ruptured the Lijiang (R3) seismic belt on February 3, 1996. Parallel to R3, the Yongshen-Ninglang-Muli-Juilong seismic belt (R4) is related to a historical event of M 7.8 in 1515. There have been a number of large earthquakes (e.g. the 1970 Ms 7.8 Tonghai earthquake) that have occurred along the Tonghai-Shiping seismic belt (R5).

Figure 12 shows the epicenter distribution for all the 5144 events relocated in this study for the period from 1999 to 2004. For comparison, we zoomed in on a subregion to show catalog locations and relocated earthquake locations (Figure 14). In general, the seismicity pattern illustrated by the original catalog locations is diffuse and is very likely biased. The original catalog depths for many events are set to zero due to the lack of constraints in the depth estimation. A much sharper image of the seismicity is obtained after relocation as shown in Figure 14. From Figure 12 we can see that the majority of events are distributed on the five seismic belts discussed above. We can identify many clear linear features and clusters, which are hard to identify in the original locations. Figure 15 shows the focal depth distribution for all the relocated events. From the figure, we can see that the number of events increases with depth from -2 to 12 km, peaks around 12 km and then gradually decreases. Some of the events shallower than 2 – 3 km below surface may well be quarry blasts. The majority of events are located within the depth range from 5 to 20 km. This range likely represents the seismogenic zone in the region. Yang et al. (2005) also reported that most of the events in the region are shallower than 20 km. However, there are many more events above 5 km in their results. The average crustal thickness in the region is about 45-50 km. It is evident that almost all the events in the region are crustal events and most of them occur within the upper crust. In the following we will discuss the hypocentral distribution for three seismic belts and an aftershock cluster in the region.

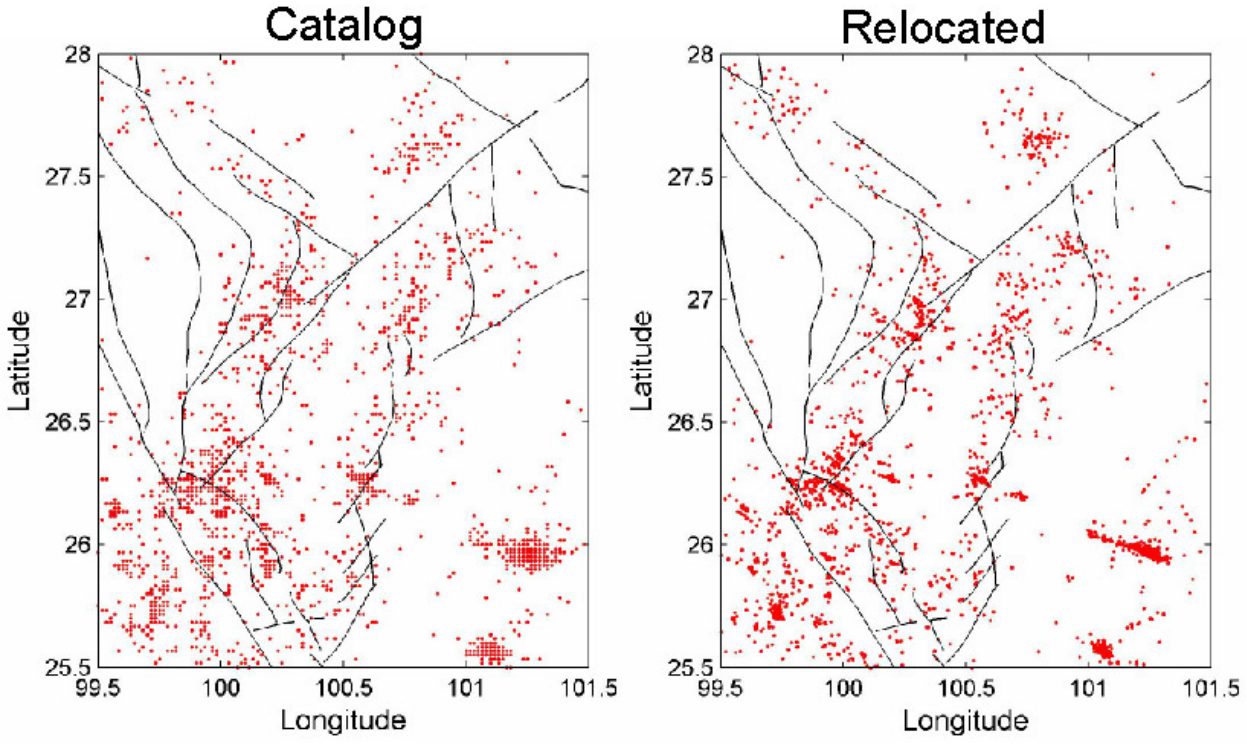

Figure 14. Comparison of catalog and relocated event locations.

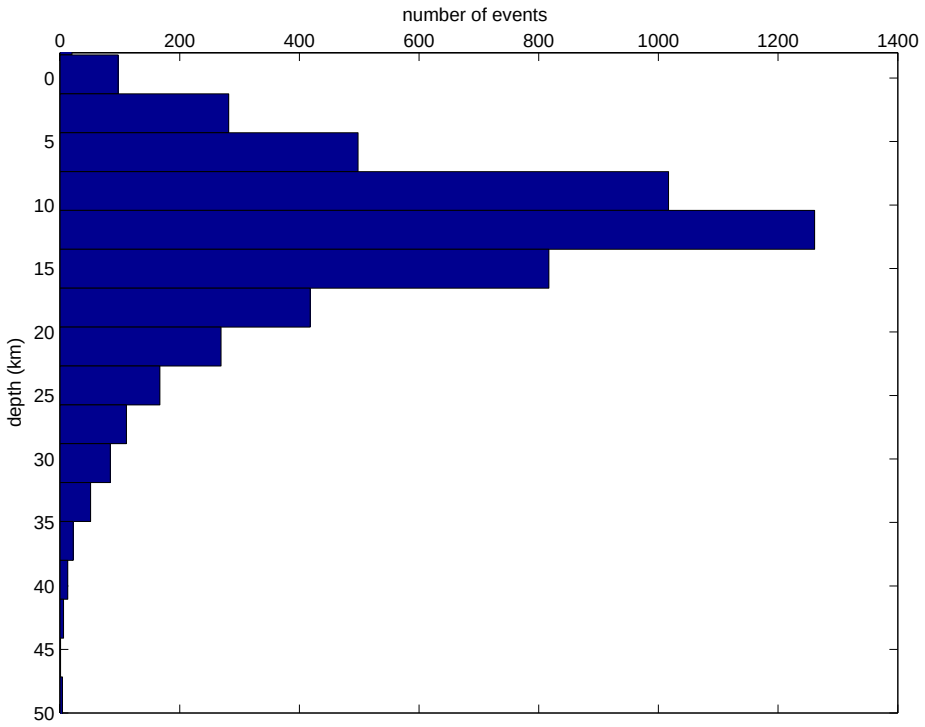

Figure 15. Focal depth distribution for all the relocated events in the Yunnan region.

Lancang-Gengma seismic belt (R2)

Figure 16 shows the relocated seismicity along the Lancang-Gengma seismic belt. Most of the events are located on the southwest side of the surface fault traces. The focal depth distribution of events along the cross section (A-B in Figure 16a) displays a slight SW dip. It is consistent with the SW-trending fault dips of ~77^{o} -79^{o} revealed by focal mechanisms of two large earthquakes (Yang et al 2005, and references therein). The focal depths are centered in the 10-15 km depth range. There are only a few events deeper than 25 km in the area.

Lijiang seismic belt (R3) and Yongshen-Ninglang-Muli-Juilong seismic belt (R4)

The Lijiang and Yongshen-Ninglang-Muli-Juilong seismic belts are two parallel active seismic belts within the Sichuan -Yunnan rhomboid-shaped tectonic block. The Lijiang seismic belt was previously described to be N-S trending and bounded by the Lijiang basin (Yang et al., 2005). More events along the northeast part of the fault zones are relocated in this study, as shown in Figure 17a. This belt could be extended further towards the northeast along the strikes of the fault traces. Parallel to R3, the Yongshen-Ninglang-Muli-Juilong seismic belt runs northeast from 26.2^{o} to 27.2^{o}N and beyond. The northern segment of the belt is out of the study region. These two NE running belts are consistent with the strikes of major faults in the area. There are no surface fault traces around the segment of the belt above 26.8^{o}N. The seismicity in this part of the belt likely illustrates a blind active fault. We can find a clear seismicity gap between these two belts. From Figure 17b, the gap can also be found in the focal depth distribution along the cross section (A-B). The majority of the events in these two belts are within the focal depth range of 5-20 km.

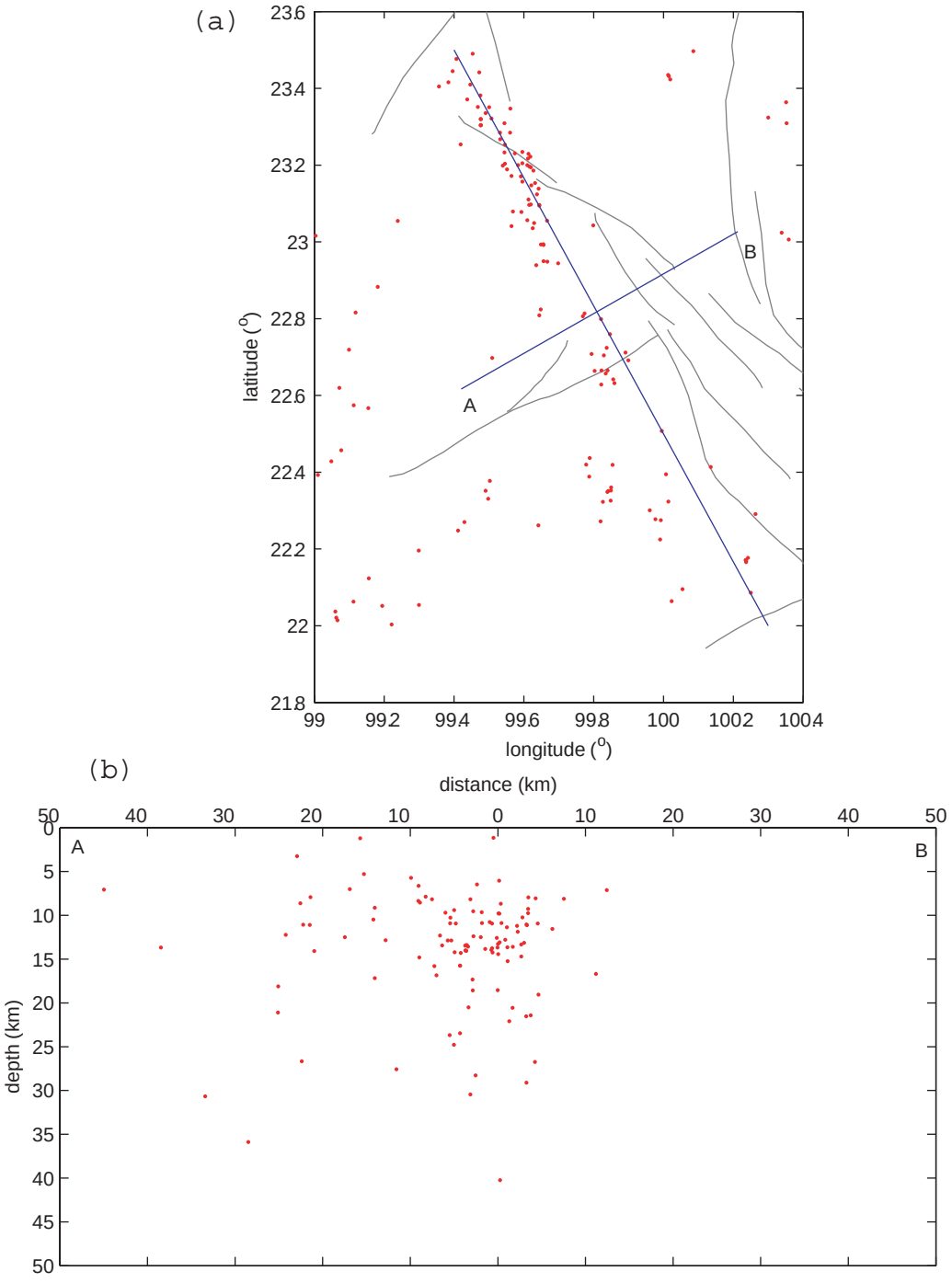

Figure 16. Hypocentral distribution of relocated seismicity (1999-2004) along the Lancang-Gengma seismic belt. (a) Epicentral distribution of the relocated events. (b) Focal depth distribution along the vertical cross section indicated by A-B in (a).

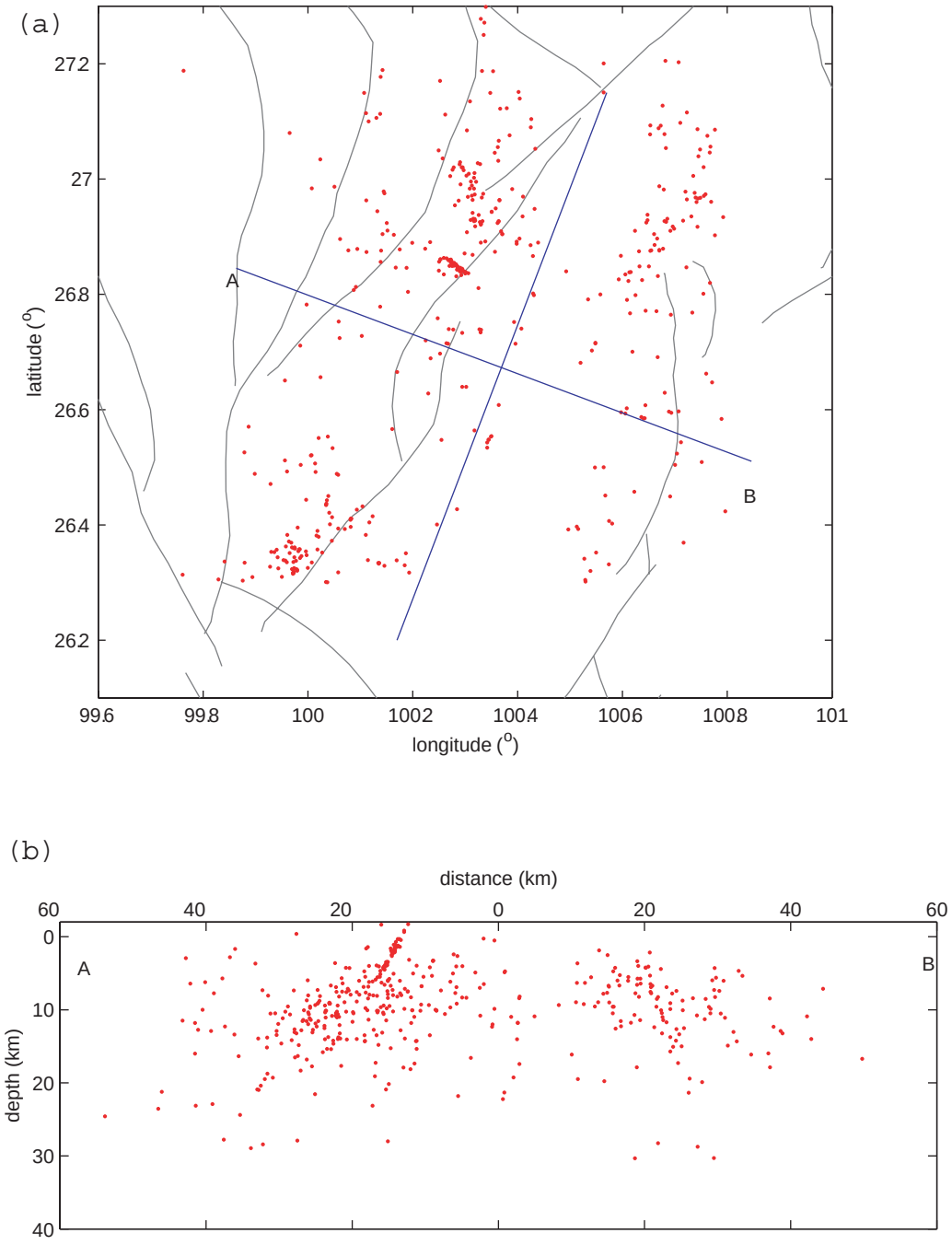

Figure 17. Hypocentral distribution of relocated seismicity along two parallel belts, Lijiang seismic belt (R3) and Yongshen-Ninglang-Muli-Juilong seismic belt. (a) Epicentral distribution of relocated events. (b) Focal depth distribution along the vertical cross section indicated in (a) by A-B.

An aftershock cluster adjacent to R3

We can identify many earthquake clusters from the relocated seismicity. One of the large clusters is located just south of the Lijiang seismic belt. There are more than 160 events distributed in about a 5km x 10km area and extending from 8km to 24 km in depth (Figure 18). Since these events occurred within several days, they are likely the aftershocks of an M 6 earthquake that took place on November 22, 2003. The narrowly distributed event locations for the cluster indicate that the accuracy for relative locations in this study could be much less than a few kilometers.

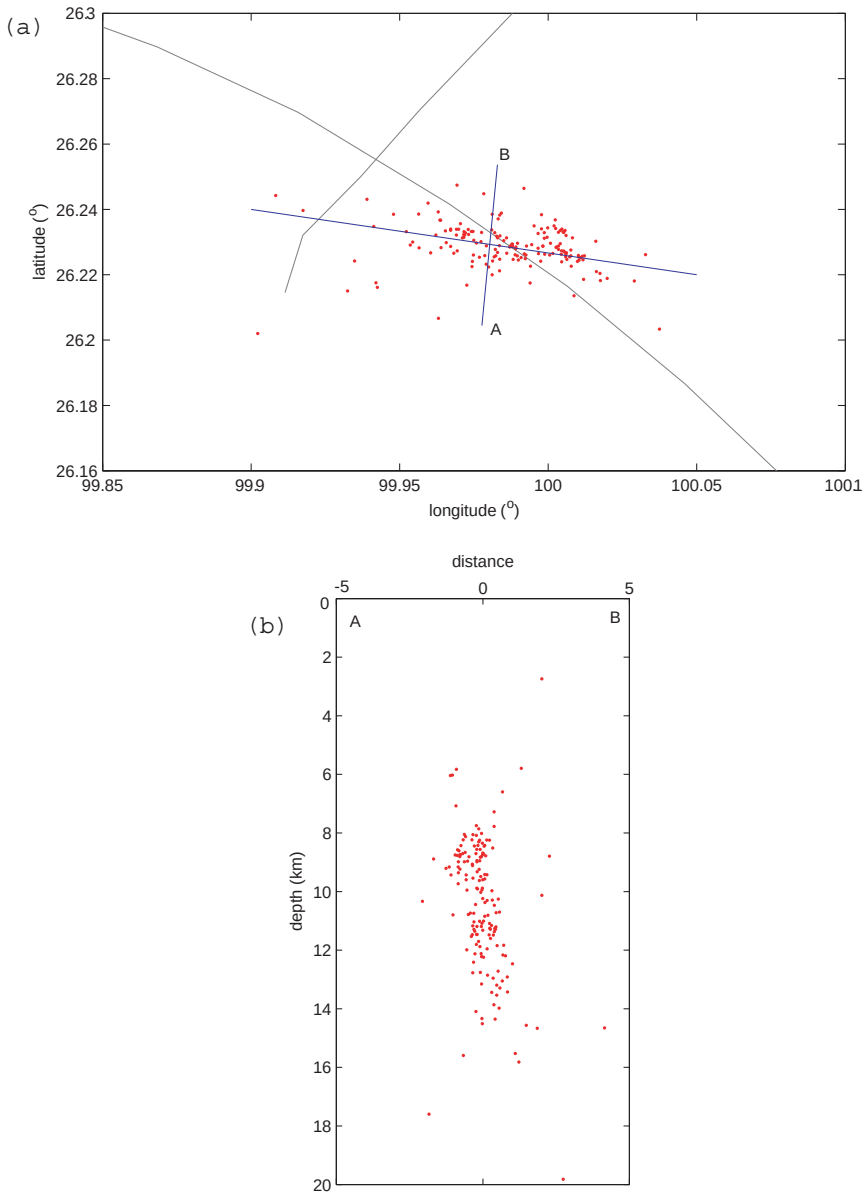

Figure 18. Relocated hypocentral distribution of an earthquake cluster. (a) Epicentral distribution of relocated events within the cluster (b) Focal depth distribution along the vertical cross section indicated in (a) by A-B.

Vp and Vs models

Figure 19 shows horizontal slices of the 3D P-wave velocity model at depths of 0, 5, 10, 15, 20, 25, 30, 40 and 45 km. These horizontal slices show strong lateral velocity heterogeneities, consistent with the nature of active fault zones in this region. Strong velocity contrasts are evident across major faults, such as the Xiaojiang Fault and Red River Fault, as shown in the W-E cross-sections of the Vp model (Figure 20). Similar features can also be found in the horizontal slices and cross-sections of the 3D S-wave model shown in Figures 21 and 22.

At shallow depths (0-5km), the distribution of low and high velocity zones is closely related to variations in thickness of the sedimentary layer and the regional geology. There is a low velocity anomaly zone to the west of longitude 99^{o}, along the Zhongdian-Lijiang-Yunlong-Wanding zone (Figures 19 and 21). Deep Seismic Sounding (DSS) studies showed about 3 km of sediments along this zone (Hu et al., 1986; Lin et al., 1993). Between the Tonghai-Chuxiong Fault (F8) and the Nujiang Fault (F4), there is a large low velocity anomaly where sediments are 1-3 km thick (He et al., 2005). This region is located around the junction of the Yangtze platform, the South China fold system and the Sanjiang fold system and large tectonic movement is expected. To the east of the Lancangjiang Fault (F4) and between latitude 25^{o} and 28^{o}N, there is a large high velocity anomaly zone where the sedimentary layer is very thin (He et al., 2005). At the depth of 10 km, the high and low velocity anomaly zones are similar to those shown at shallow depths. The shape of the high velocity zones changes very little from the surface to the depth of 10 km.

Starting from the depth of 15 km, we see low velocity anomalies associated with the major fault zones, such as the Xiaojiang Fault (F1), the Tonghai-Chuxiong Fault (F8), and the Nandinghe Fault (F5). At shallower depths, the velocities around these zones are relatively higher. On the other hand, the velocity is higher along the Zhongdian-Lijiang-Yunlong-Wanding zone, indicating the basement layer velocity in this zone is higher than surrounding areas, as found from the phase velocity map (He et al., 2005). The low-velocity zone between the Wuliangshan Fault (F3) and the Red River Fault (F2) extends all the way down to a depth of around 50 km.

In the cross-sections shown in Figures 20 and 22, we can see that most of the faults are associated with a velocity contrast. In the cross-section along latitude 27^{o}N, to the west of the Nujiang Fault (F6), the velocities are lower. Between the Nujiang Fault (F6) and the Zemuhe Fault, there is a broad zone of low velocity that is the central part of the Sichuan-Yunnan rhomboid block. Most of the earthquakes are concentrated around the edge of the velocity contrast. To the east of the Anninghe Fault (F9), there is a high velocity anomaly around latitude 27^{o}N starting from a depth of 25 km. This high velocity body likely depicts the Kangdian uplift, related to an intrusion of deep material. In the cross-section along latitude 27^{o}N, there is a low velocity depression between the Lancangjiang Fault (F4) and the Red River Fault (F2). There is a cluster of earthquakes around longitude 101^{o}E and there is no fault trace on the surface around this cluster. However, we see these earthquakes are located along a velocity contrast that is higher to the east. It is likely this cluster of earthquakes is associated with a blind fault. Along the cross-section at latitude 25^{o}N, from west to east, it crosses the Sanjiang fold zone, the Dianzhong depression and the Kangdian uplift. Clear velocity contrasts are associated with the Lancangjiang Fault, the Red River Fault and the Xiaojiang Fault. Tengchong Volcano is located around longitude 98.3^{o} and to its west down to the depth of 50 km, there is a low velocity anomaly.

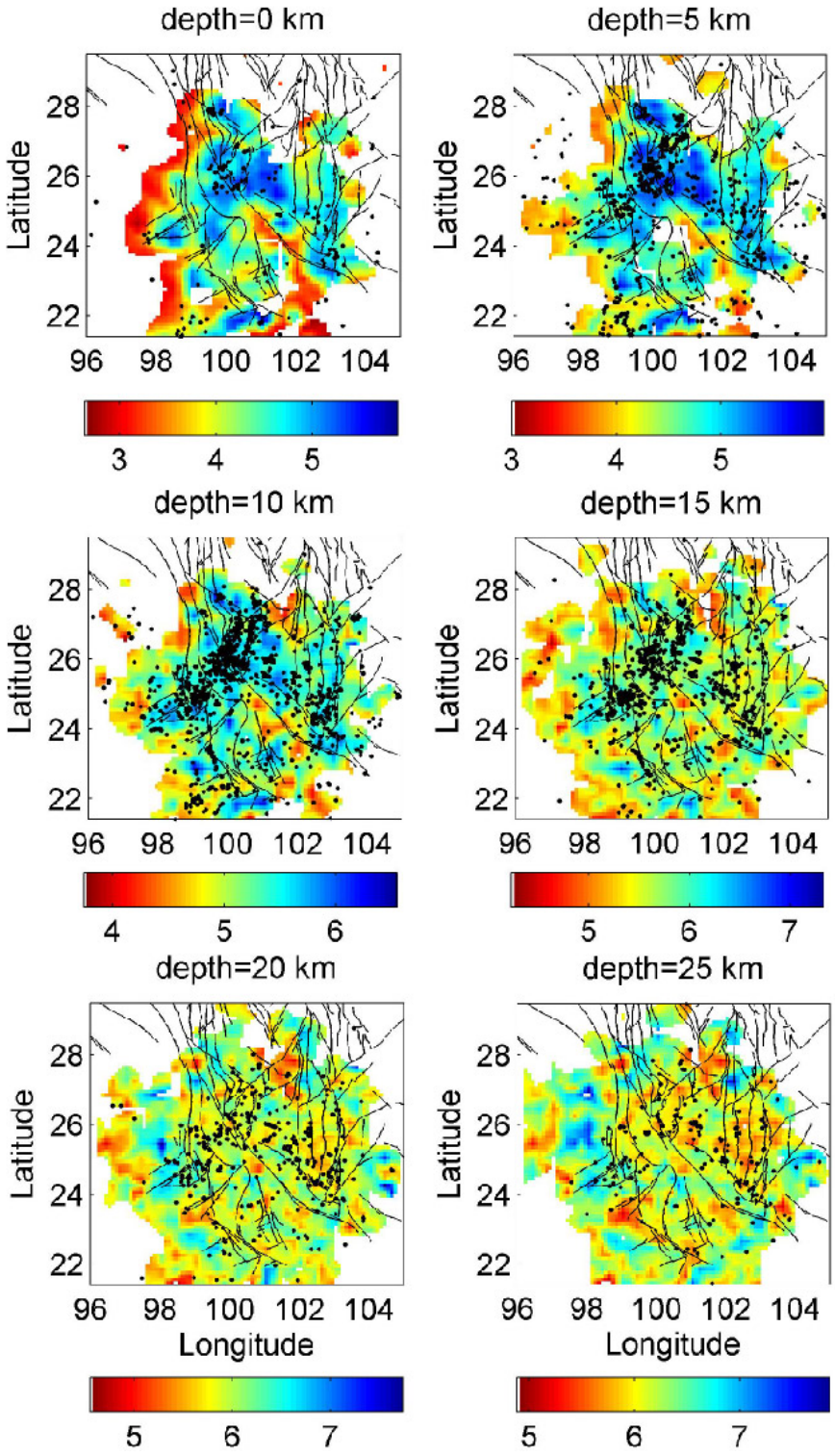

Figure 19. Horizontal slices of the three-dimensional Vp model at depths of 0, 5, 10, 15, 20, 25, 30, 35, 40, 45 and 50 km (continued on the next page).

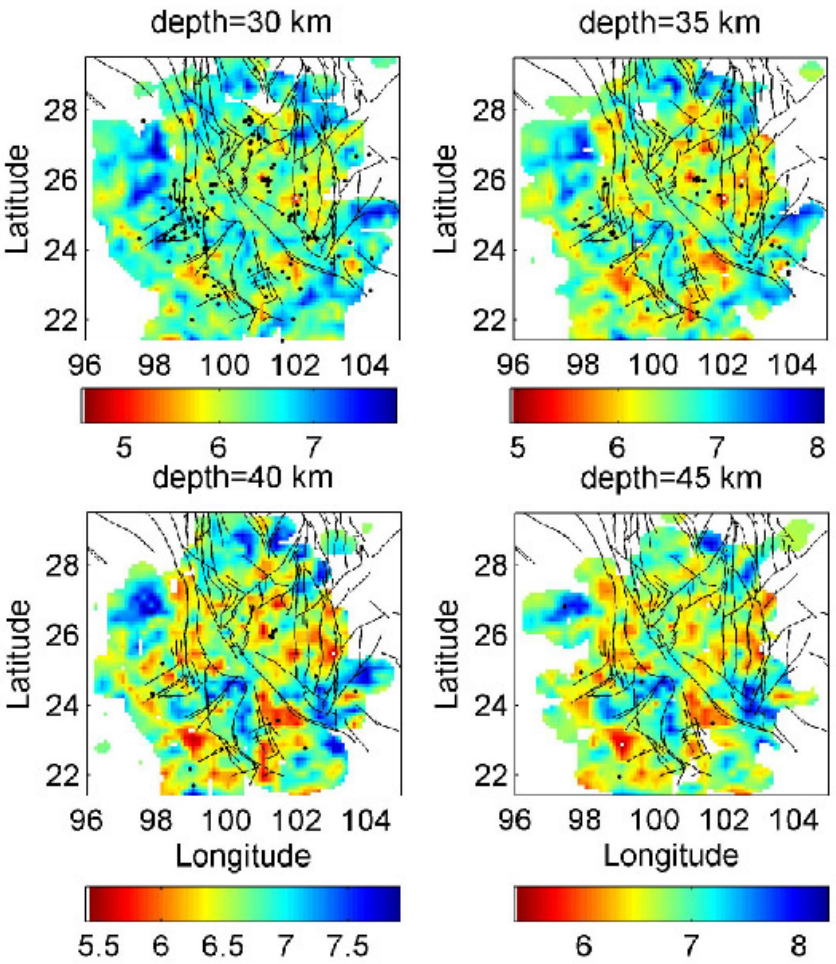

Figure 19 (continued).

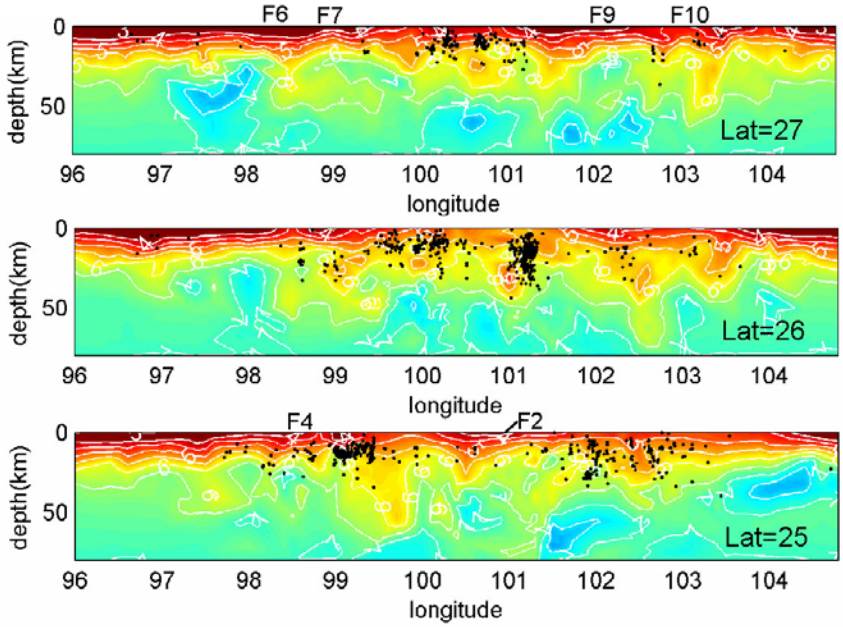

Figure 20. W-E cross-sections of the Vp model at latitudes of 27°, 26° and 25°N.

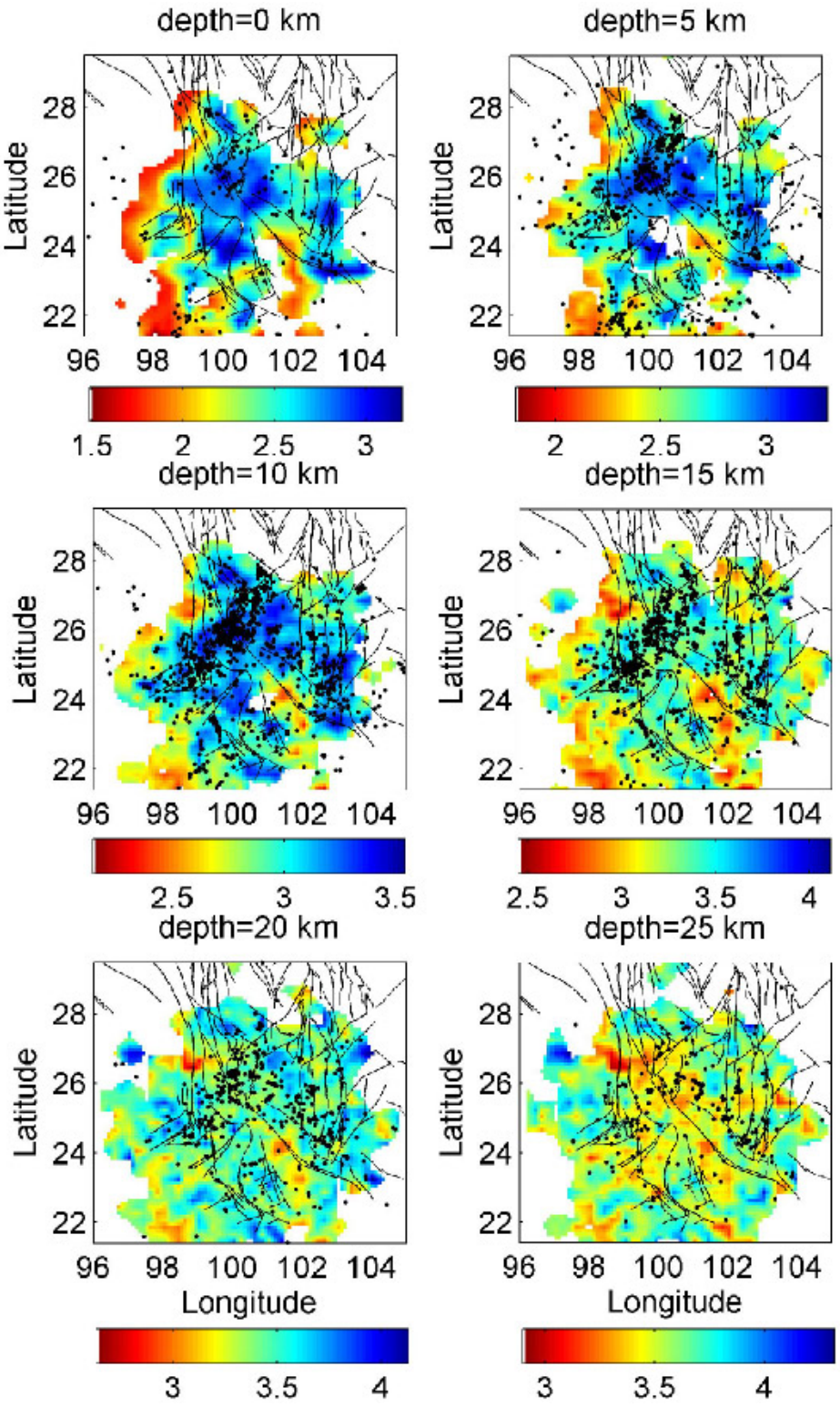

Figure 21. Horizontal slices of the three-dimensional Vs model at depths of 0, 5, 10, 15, 20, 25, 30, 35, 40, 45 and 50 km (continued on the next page).

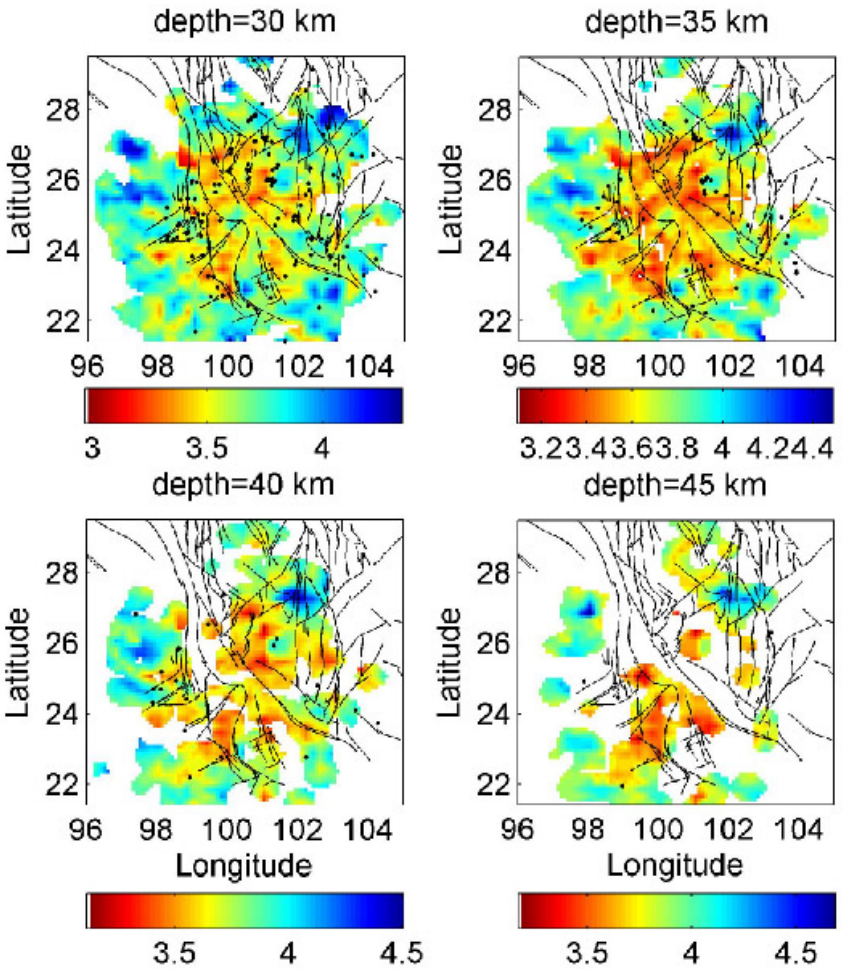

Figure 21 (continued).

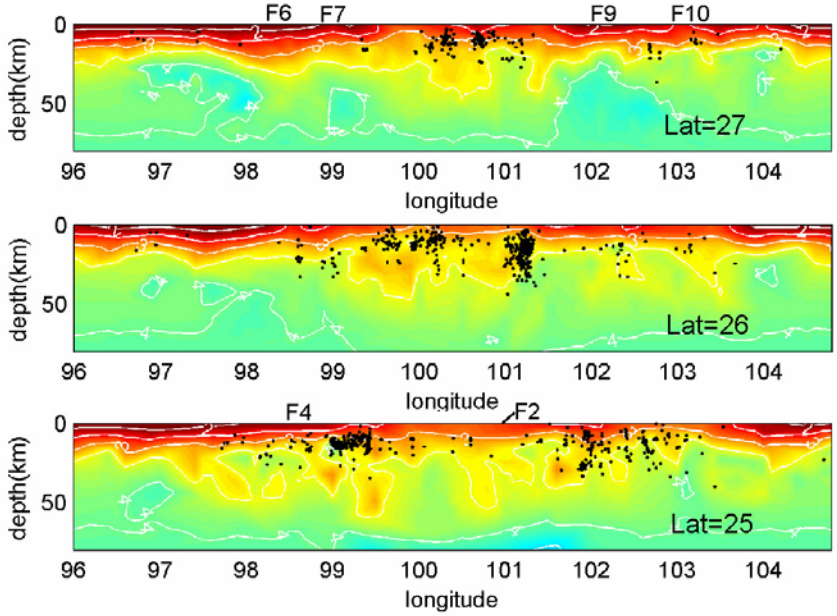

Figure 22. W-E cross-sections of Vs model at latitudes of 27^{o}, 26^{o} and 25^{o}N.

7. Earthquake locations and 3D velocity models in the Sichuan region

For the Sichuan region, we collected catalog picks for ~5000 earthquakes observed on ~50 stations. Figure 23 shows the event and station distribution in this study. Note that the earthquake locations are the final product of our seismic tomography study, not the original catalog locations. There are ~39600 P picks and ~37100 S picks in our data set. Figure 24 shows the ray path coverage for P and S waves. For the selected events, there are at least 8 observations including P and S times. From these absolute times, we constructed 280,000 P and 270,000 S differential times. The number of average links per event pair is 11. The average hypocentral separation for the linked event pairs is ~8.4 km. Though we also calculated cross-correlation times for ~300 events, they have minimal effect on final event locations and velocity models because of the limited number of observations.

We first solved for a 1D model at depths from 0 to 80 km with an interval of 5 km using the absolute P and S times. Then we used this 1D model as our initial model to simultaneously determine event locations and velocity models using both absolute and differential P and S times. The horizontal grid spacing is 0.5^{o} in latitude and longitude. The absolute and weighted arrival time RMS residuals at the beginning of the inversion are 1.877 s and 4.786 s and they decrease to 325 ms and 53 ms at the end of the inversion, respectively. Very large smoothing weight of 600 is applied because the data are noisy and the accuracy of arrival times is not good (~0.1 s).

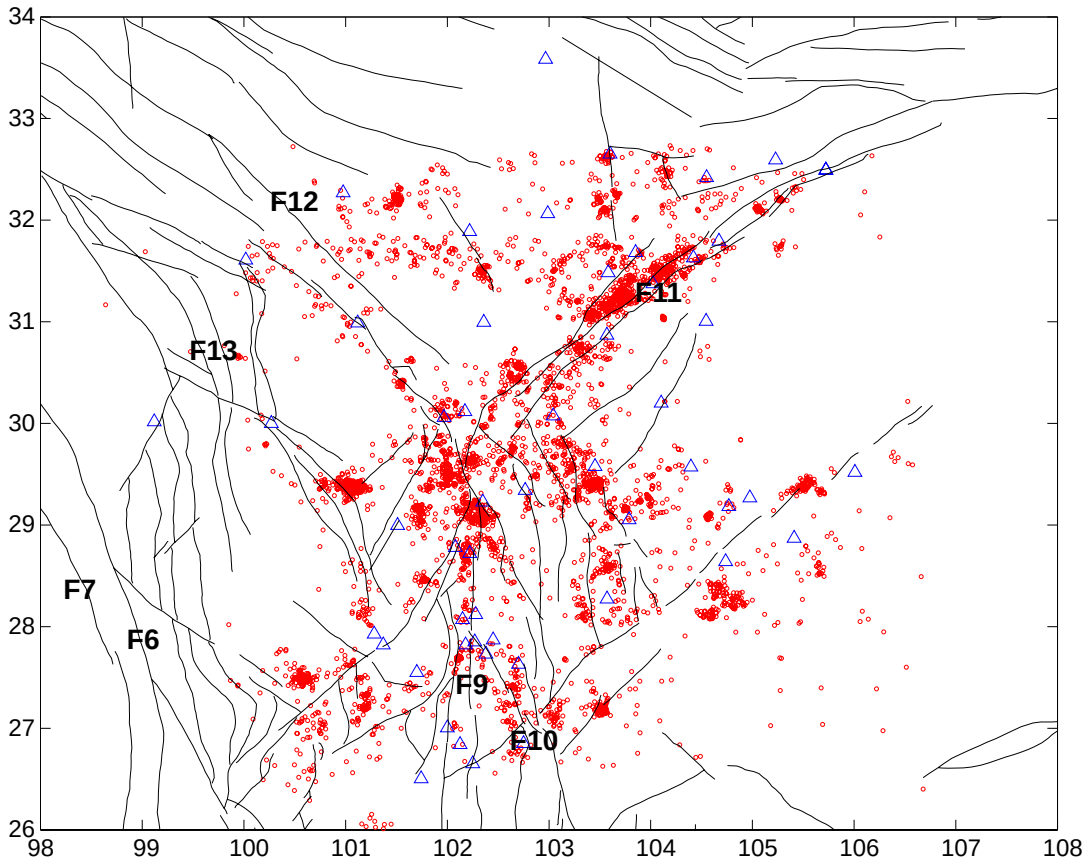

Figure 23. Event and station distribution for the Sichuan region. For fault names, refer to Figure 1.

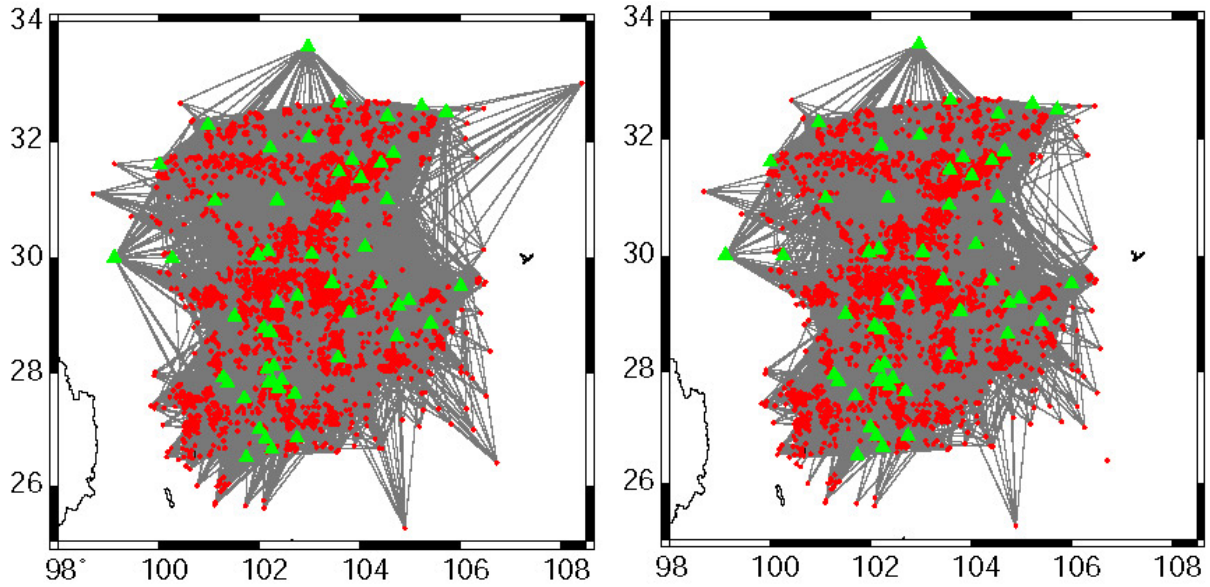

Figure 24. Ray path coverage for (left) P and (right) S waves. Earthquakes are indicated by red dots and stations are indicated by green circles.

Earthquake locations

(1) Xianshuihe seismic belt (F12)

The Xianshuihe Fault is the northeast boundary of the Sichuan-Yunnan rhomboid tectonic block. The slip rate along the fault is about 8-15 mm/yr (Su and Qin, 2001). Although a series of large earthquakes (e.g. the 1973 M 7.6 earthquake and the 1981 Ms 7.0 earthquake) occurred along the fault, the recent seismicity in the belt is relative low as shown in Figures 23 and 25. The epicentral distribution of events in this belt follows the NW strike of the fault trace well. As shown in Figure F25b, the events in the belt are usually shallower than 25 km.

(2) Longmenshan seismic belt (F11)

The Longmenshan seismic belt is the most active seismic area in the Sichuan region. As shown in Figures 23 and 26, there are many small to moderate earthquakes occurring in this ~100 km wide belt. The band clearly coincides with the NE strike of the Longmenshan Fault. No earthquakes with $M \geq 7$ have been documented in the belt. However, several $M > 6$ earthquakes (e.g. the 1657 M 6.5 Wenchuan Earthquake and the 1970 M 6.2 Dayi Earthquake) occurred along the fault historically. The focal depth distribution along the cross section A-B in Figure 26a is shown in Figure 26b. The event depths are centered on ~ 20 km and extend to ~40 km deep. Apparently, there are more deep events along the belt than the seismic belts in the Yunnan region.

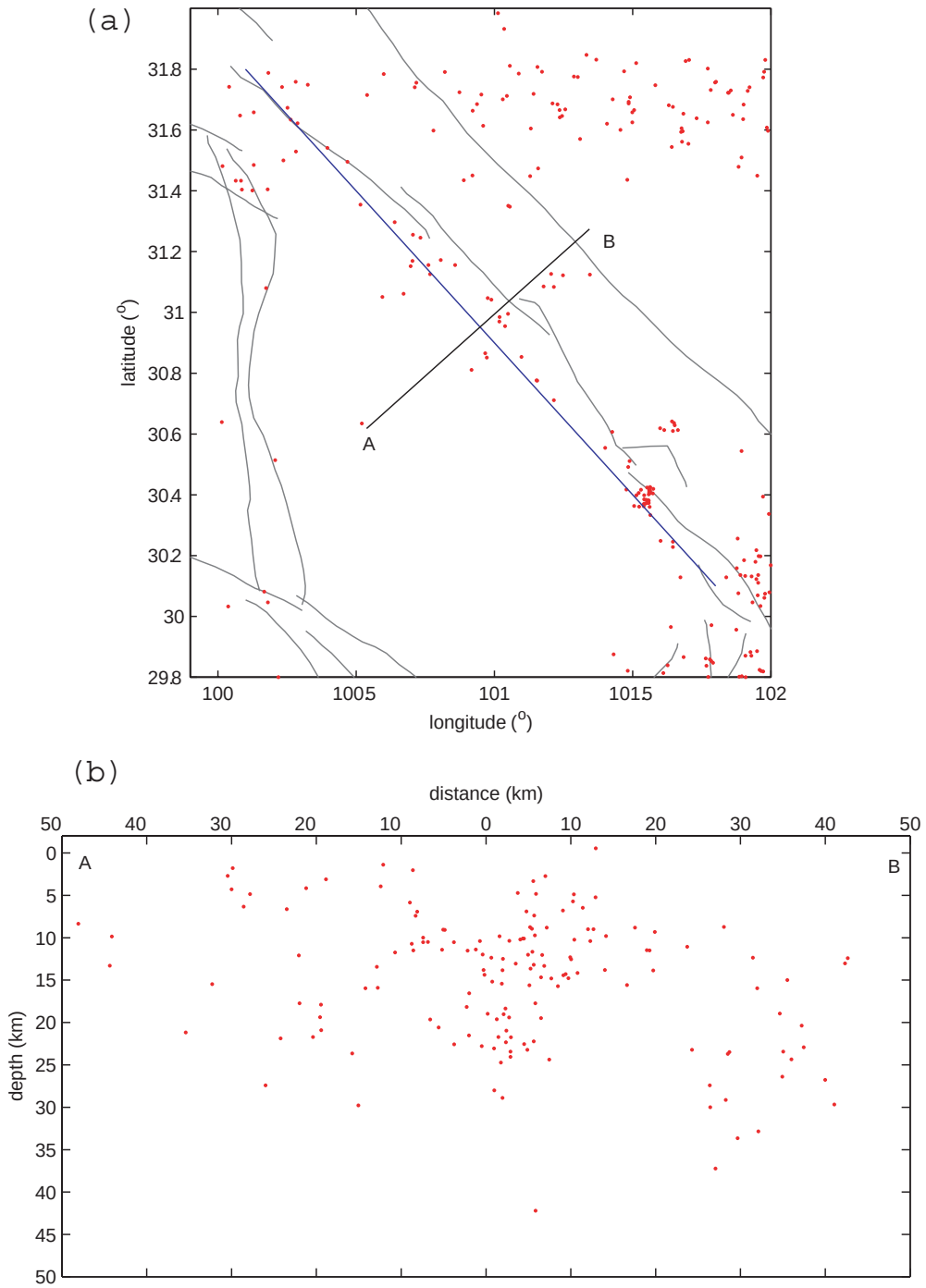

Figure 25. Relocated seismicity along the Xianshuihe seismic fault (F3). (a) Epicentral distribution of relocated events. (b) The focal depth distribution of relocated events along the cross section A-B.

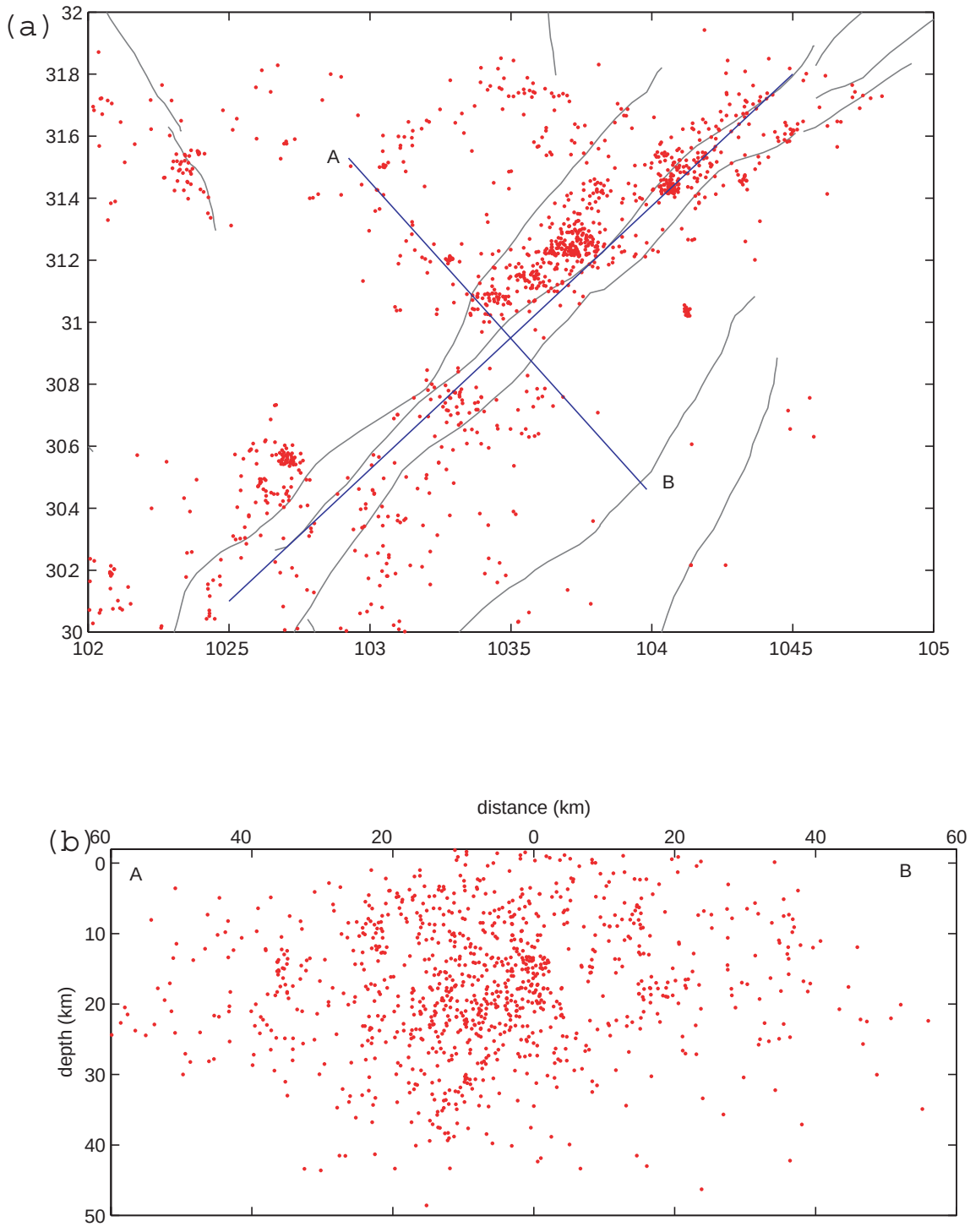

Figure 26. Relocated seismicity along the Longmenshan seismic belt (F5). (a) Epicentral distribution of relocated events. (b) The focal depth distribution of relocated events along the cross section A-B.

Vp and Vs models

Figures 27 and 28 show horizontal slices of the 3D Vp and Vs models at different depths, respectively. The regions that are not well resolved are shown as blank. Strong velocity variations can be seen in both the Vp and Vs models indicating significant structure heterogeneities in this region. At shallow depths of 0 and 5 km, we see clear low velocity anomalies associated with the Sichuan Basin to the east, the northern end of Xianshuihe Fault to the west, and the southern end of the Xianshuihe Fault and the northern end of the Anninghe Fault. There are few earthquakes occurring in these low velocity anomaly zones. The Longmenshan Fault separates a positive anomaly to the west and a negative anomaly to the east. A high velocity anomaly corresponds to Minshan-Longmenshan upwarping and Maerkang upwarping (Xu et al., 1985). The Longmenshan Fault is considered as a tectonic boundary between the Songpan-Garze Fold system to the west and Yangtze Craton to the east. The Songpan-Garze fold system is composed of slightly metamorphosed rocks thrust over sedimentary formation in the Yangtze Platform (Ren et al., 1980; Wang et al., 2003). There is also an evident high velocity anomaly located around latitude 30^{o} and longitude 102^{o} from Panzhihua to Xiangcheng. This high velocity anomaly likely corresponds to a passively reactivated ancient rift zone (Teng, 1987; Huang et al., 2002), which contains mainly metamorphic complex and basic and ultra-basic rocks that are considered to consist of high density upper mantle materials (Xu et al., 1985).

At depths of 10 to 20 km, strong low velocity anomalies are still associated with the Xianshuihe Fault and the northern segment of the Anninghe Fault. However, the Longmenshan Fault zone is associated with high velocity anomalies. Most of earthquakes are located on the boundary between high-V and low-V zones.

At deeper depths of 25 to 35 km, strong low velocity anomalies are located in the southern and northern parts of the study areas corresponding to the Xianshuihe Fault and the Anninghe Fault zones, but are separated by the Longmenshan Fault. This low velocity anomaly is likely caused by high temperature anomalies and fluid reservoirs (Huang et al., 2002) and may be weakened by the uplifting and folding due to Indo-China movement. On the other hand, the velocities are higher underneath the Yangtze Platform that is more stable.

The low velocity zones associated with the southern segment of the Xianshuihe Fault and the northern segment of the Anninghe Fault continue to a depth of 45 km. In fact, the low velocity anomaly still exists at least down to the depth of 65 km. This result is consistent with the low Vp anomaly beneath southeast Tibet from the teleseismic P-wave travel time tomography (Li et al., 2006) and the low phase velocity or S-wave velocity beneath southeast Tibet from ambient noisy tomography (Yao et al., 2006). This low velocity anomaly may be related to lower or middle crustal flow in the geodynamical models by Royden et al. (1997) and Beaumont et al. (2004). These low velocity zones may cause the weakening of the seismogeneic layer in the upper crust and thus the large earthquakes are more likely to happen due to the effect of the tectonic stress (Zhao et al., 2000).

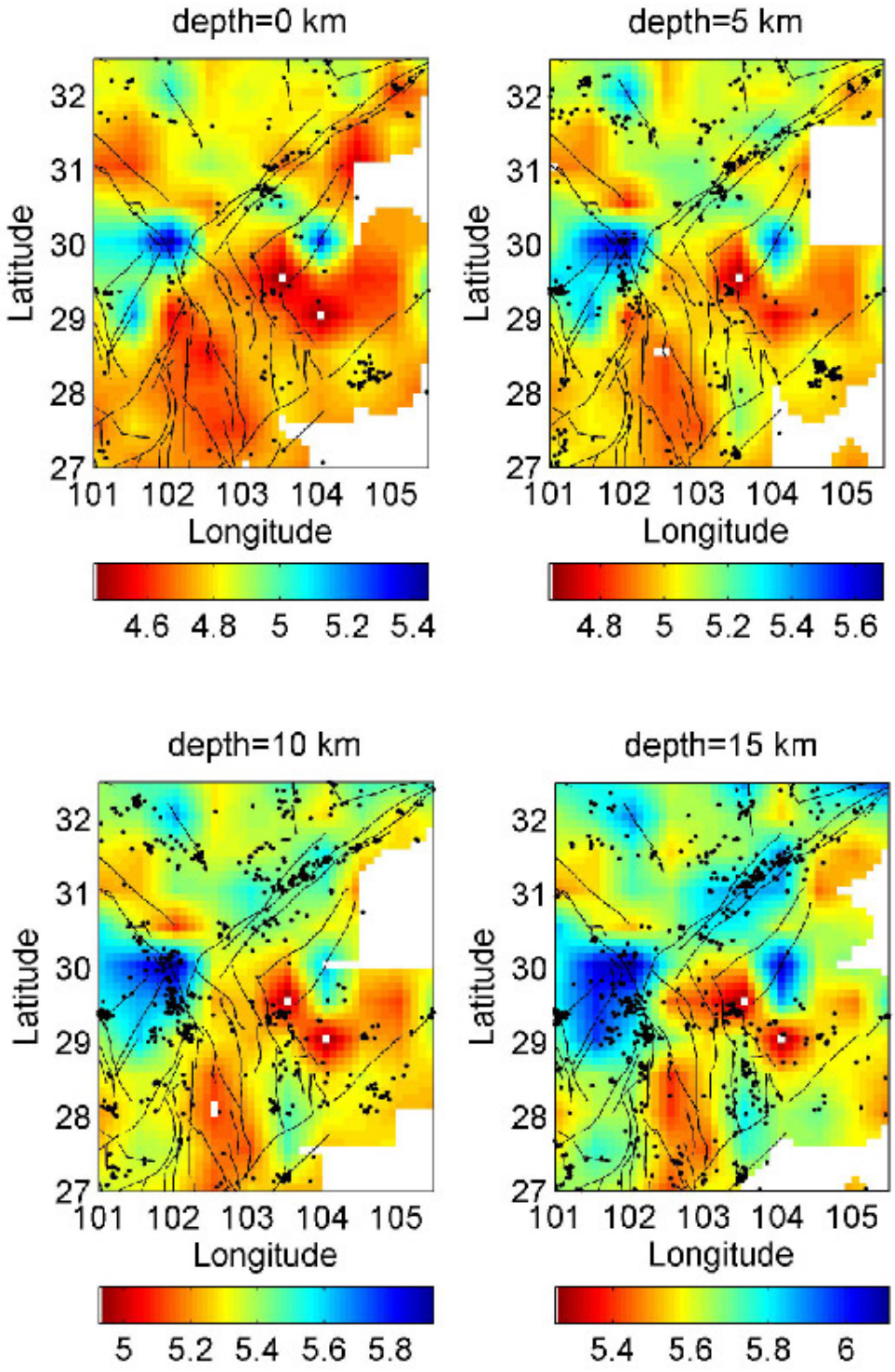

Figure 27. Horizontal slices of the 3D Vp model at depths from 0 to 75 km at an interval of 5 km (continued).

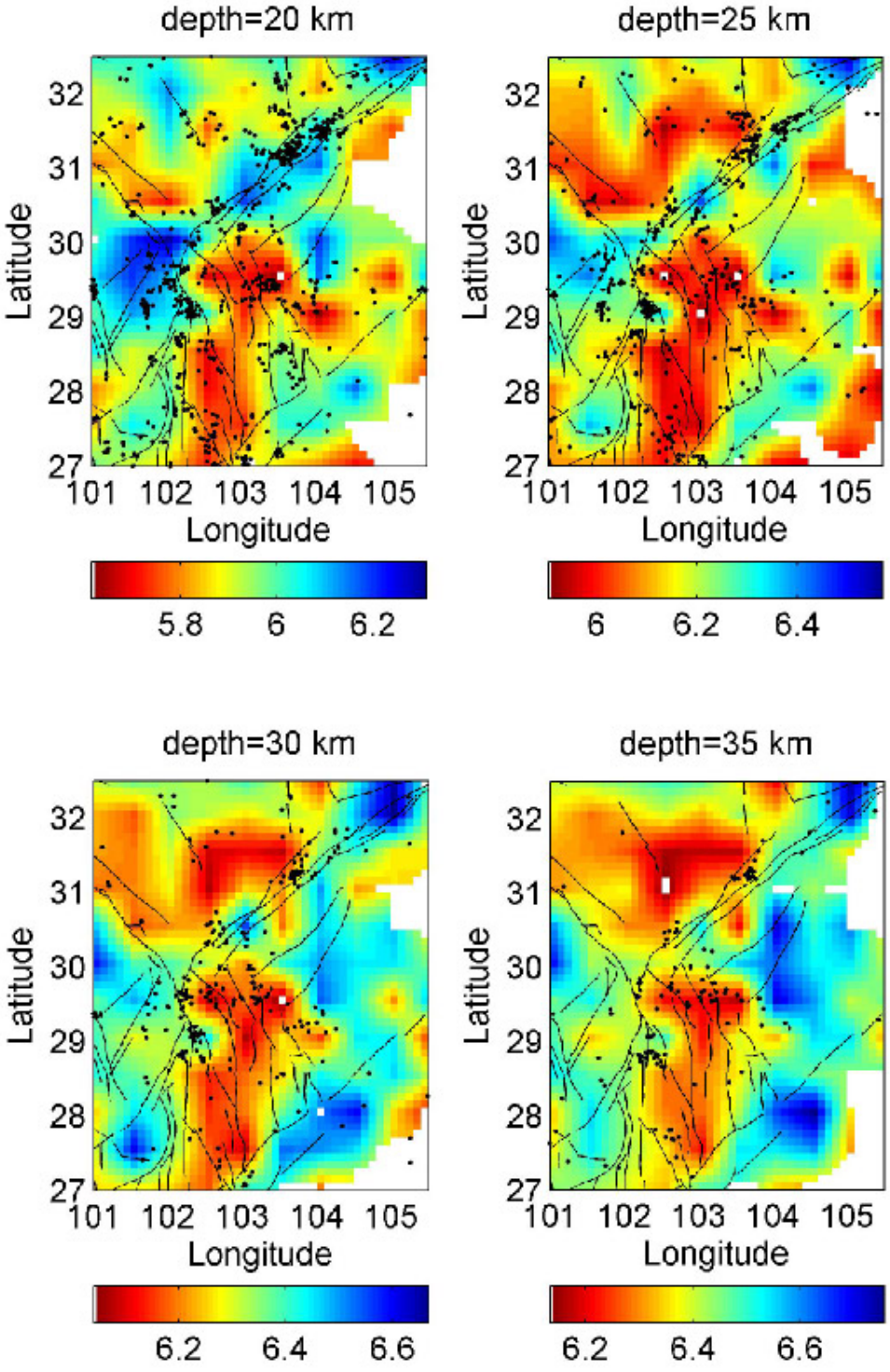

Figure 27 (continued).

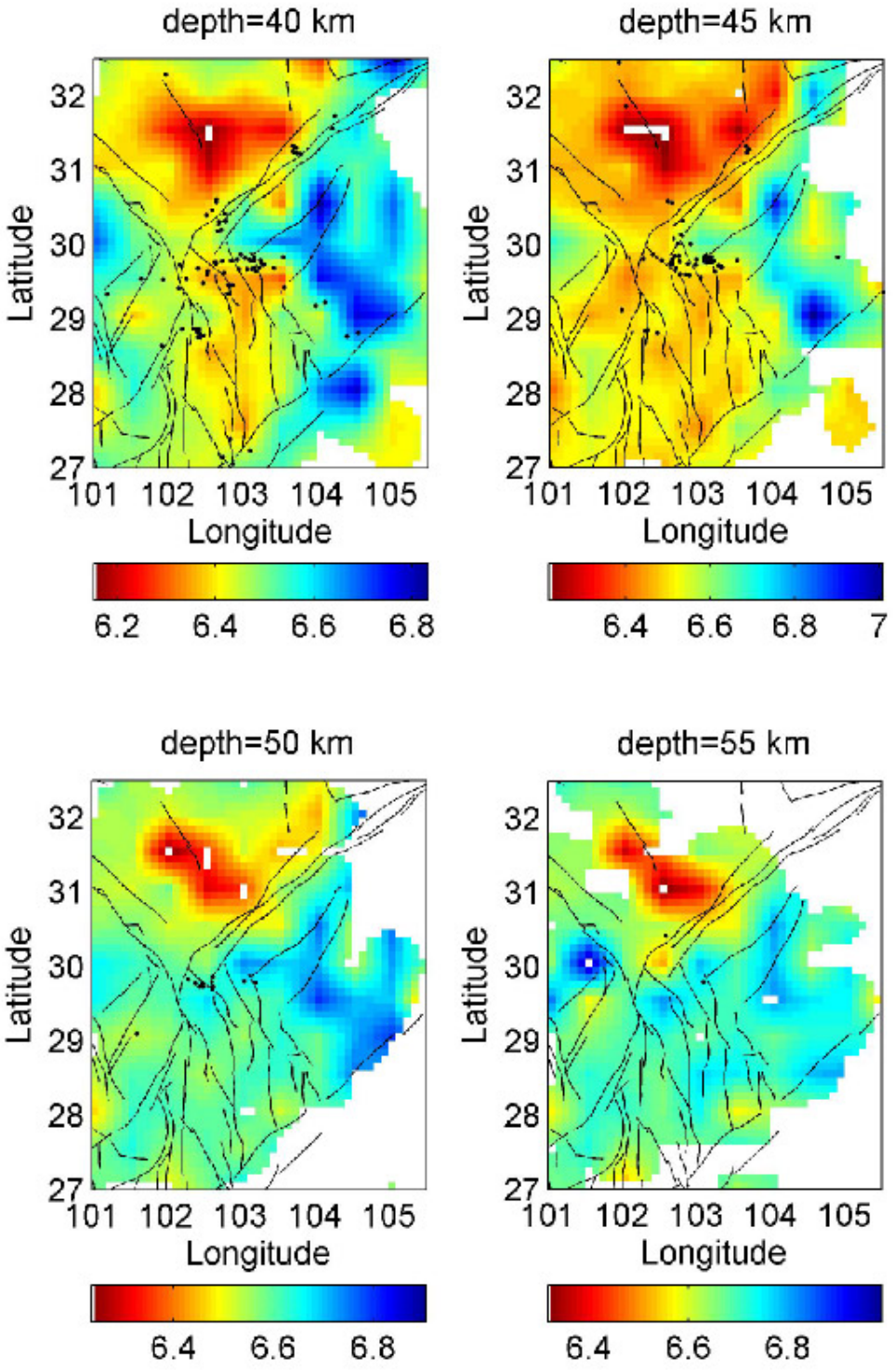

Figure 27 (continued).

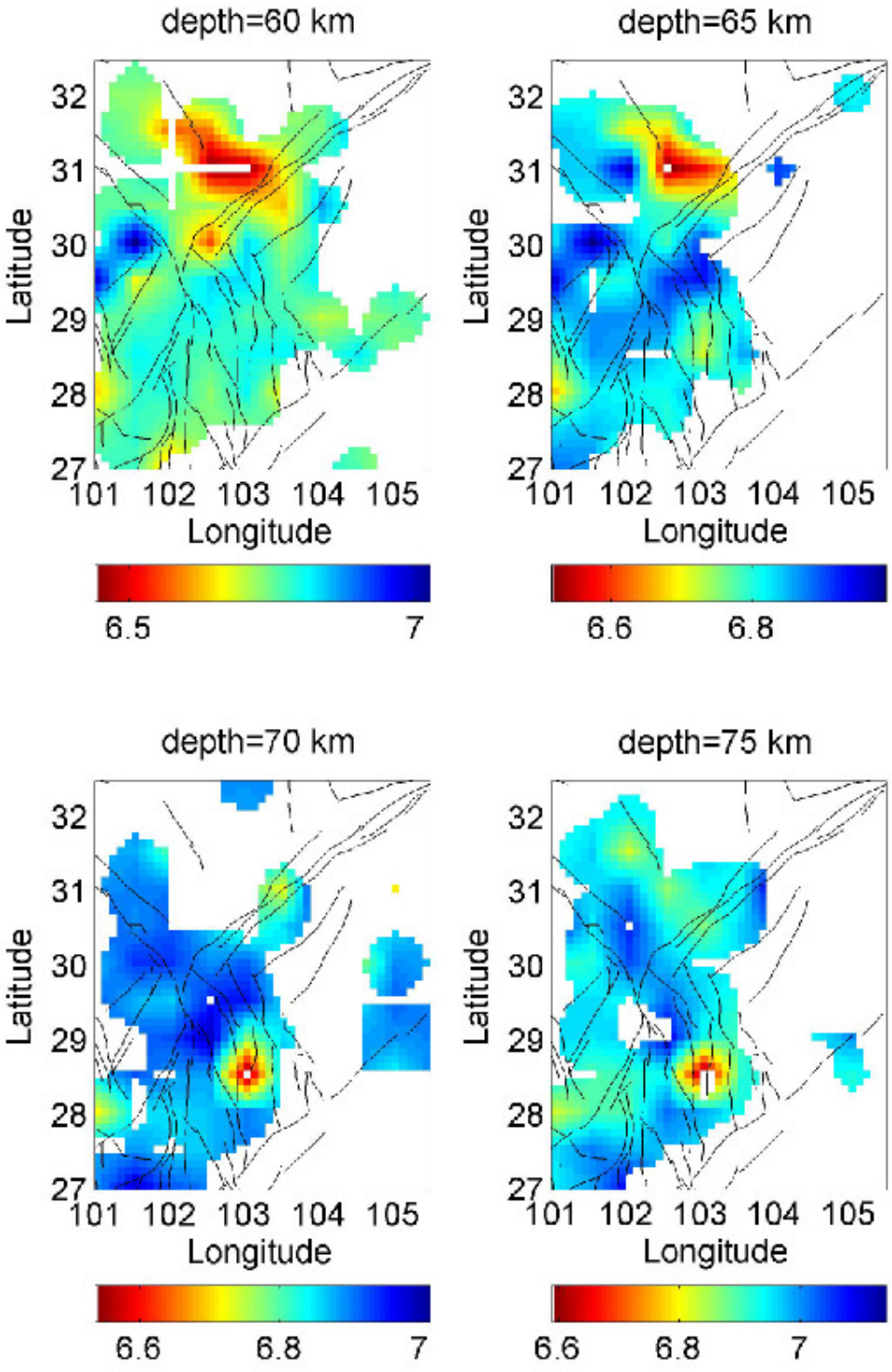

Figure 27 (continued).

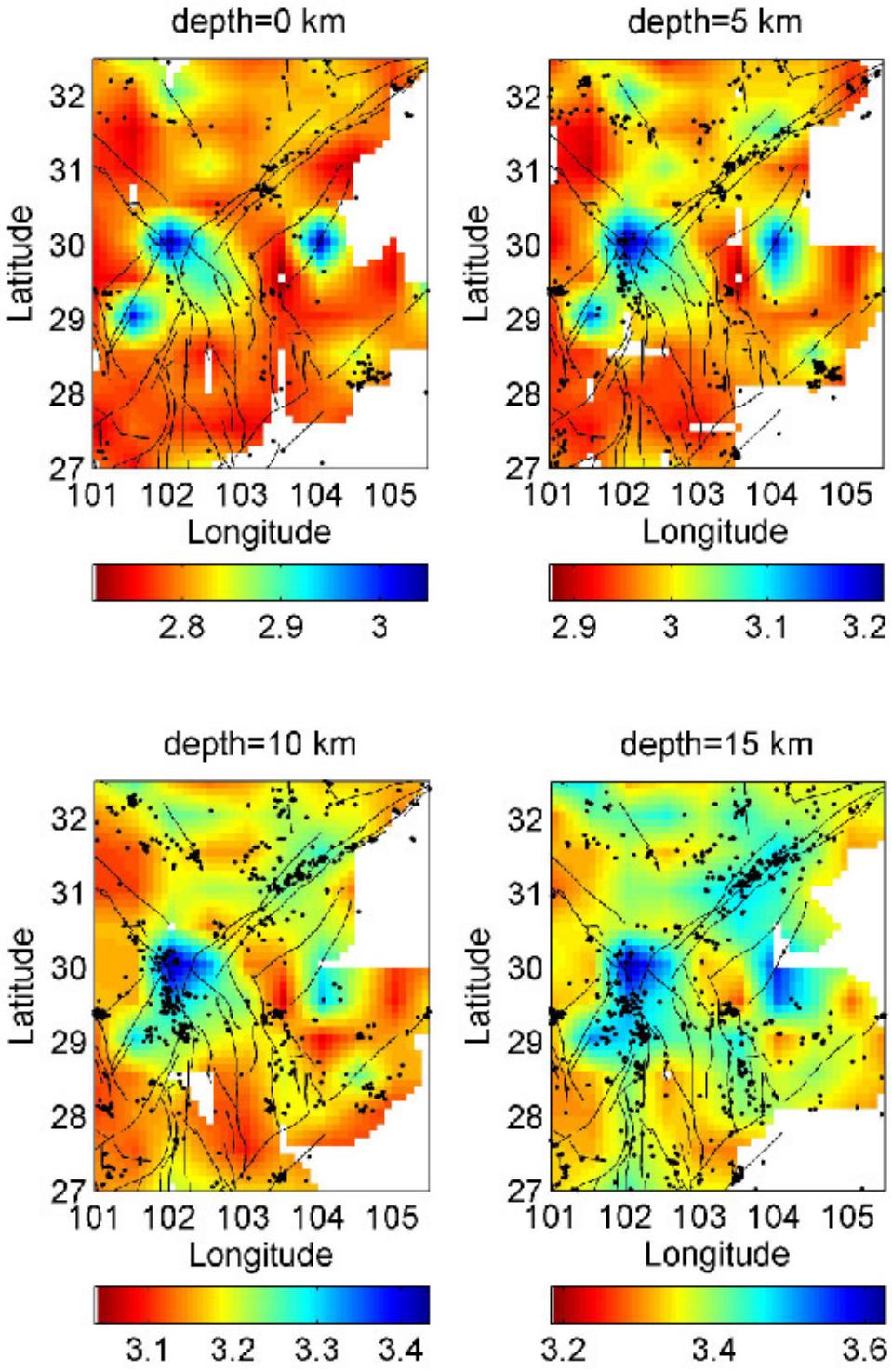

Figure 28. Horizontal slices of the 3D Vs model at depths from 0 to 45 km at an interval of 5 km (continued).

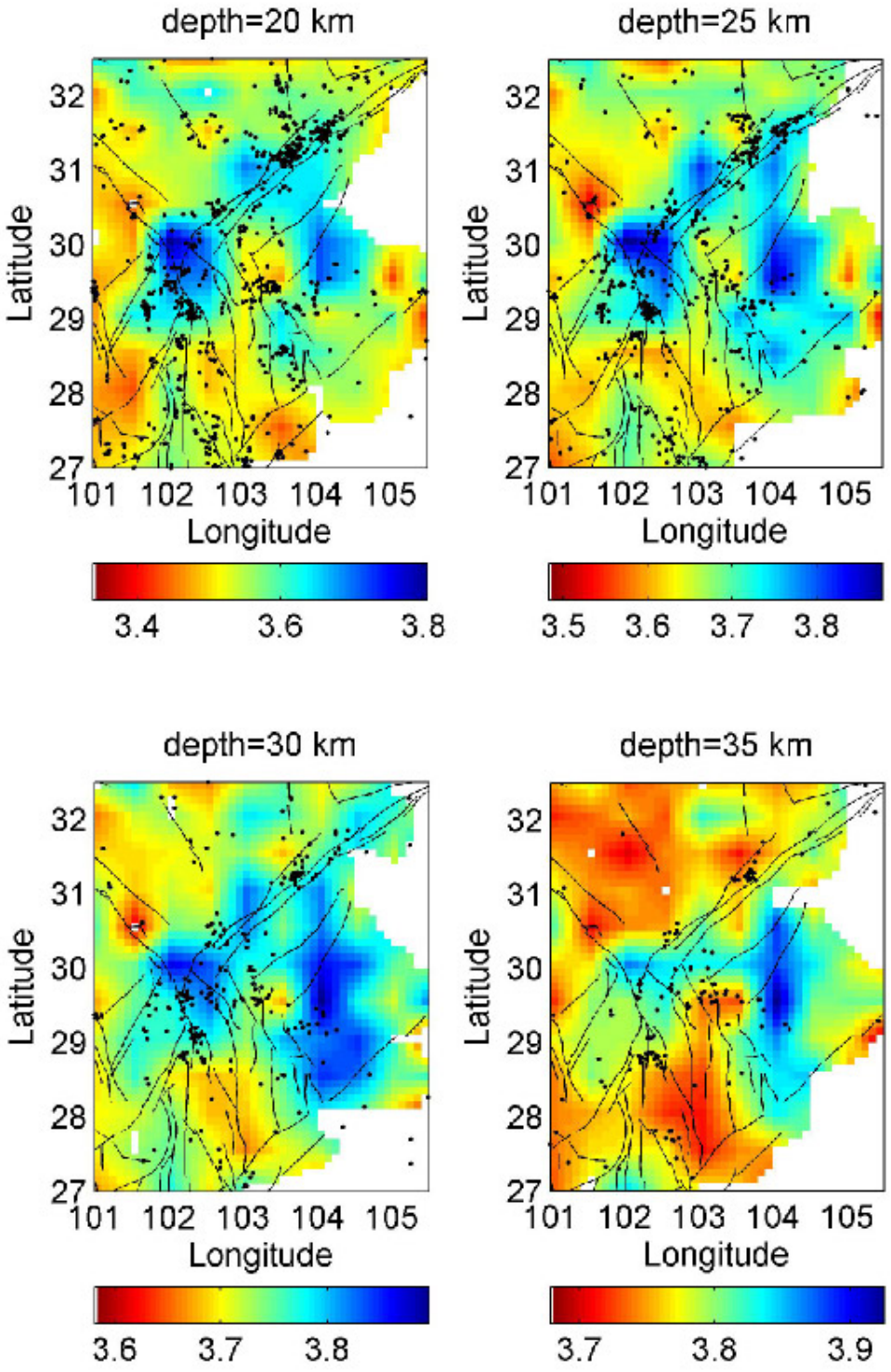

Figure 28 (continued).

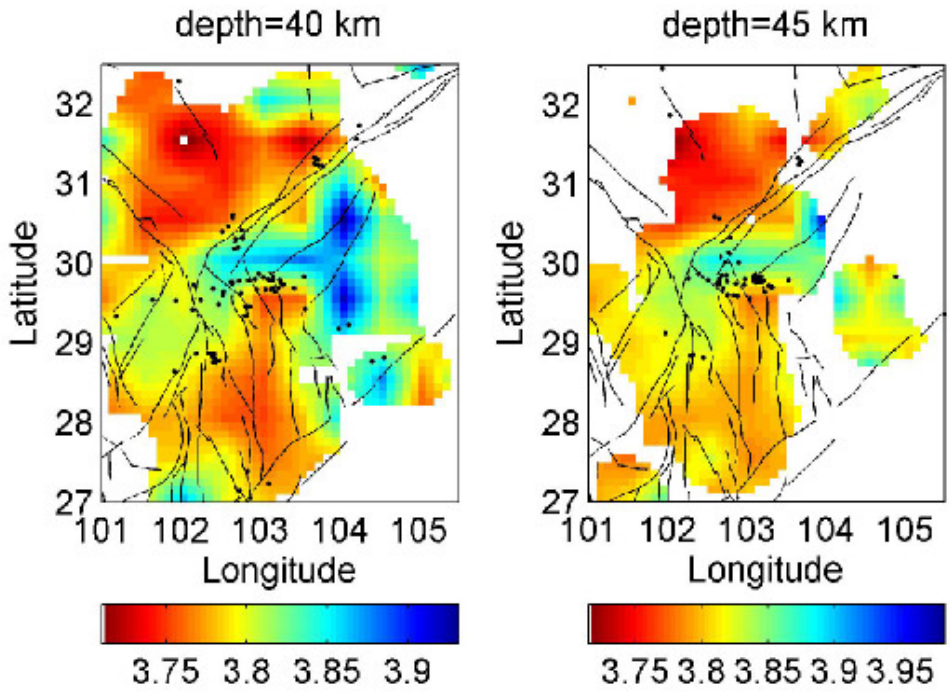

Figure 28 (continued).

8. Seismic attenuation models for the Yunnan region

Generally, the attenuation tomography system is solved using an iterative method in which the Q model is updated according to t* residuals from an initial Q model. We found out the Q values could be negative and they also depend on the starting Q values to some extent. Once the event locations and the velocity model are known, the relationship between t* values and the reciprocal Q structure (1/Q) is linear as shown in Equation (2). For this reason, we modified the program by using a nonnegative least squares (NNLS) algorithm (Lawson and Hanson, 1974) to directly solve the system for 1/Q without iterations. This method guarantees that the Q values are nonnegative and not dependent on the initial values. As noticed by Roth and Wiens (1999), the NNLS algorithm may yield some very high Q values but the nonnegative constraint removes the negative models that are not realistic.

We first use the ~10200 P-wave t* values estimated from an Ω-square source model from ~3000 events on 26 stations. The horizontal and vertical grid intervals are 0.5^{o} and 10 km. The velocity model and event locations are taken from the previous velocity tomography results. Similar to the velocity tomography, smoothing and damping are applied to regularize the inversion system but the smoothing is applied to neighboring 1/Q values, not perturbations. Smoothing weight and damping values are selected based on trade-off curves between data variance and model variance. The RMS t* value is 0.0294 and after the inversion the RMS t* residual is 0.0101, indicating the t* values are successfully fit to about 2/3 of their true values with the resulting Q models.

Figure 29 shows horizontal slices of the 3D Qp model at depths of 0, 10, 20, and 30 km. At the

depth of 0 km, the Qp values are generally low indicating relatively high attenuation because of sediments near the surface. At the depth of 10 km, we can see high Qp values correlate relatively well with high velocity anomalies where the sedimentary layer is thin, as shown in Figure 19. There is a low-Qp zone between the Red River fault (F2) and the Wuliangshan fault (F3), extending to a depth of at least 20 km, consistent with thick sedimentary layers in the region. The Kangdian uplift to the east of the Anninghe Fault (F9) also shows high Qp anomalies related to an intrusion of deep material.

We then updated this Qp model using differential t* values measured from a least squares line fitting to spectral ratios for two events and two stations. There are ~127000 differential t* values corresponding to ~1550 events and 23 stations. For the triple difference attenuation tomography method, only regions near the sources and stations are resolved because rays for two events and two stations overlap in the regions away from events and stations. For this reason, we used the Qp model from conventional attenuation tomography as an *a priori* model in the triple difference attenuation tomography. Figure 30 shows horizontal slice of the new Qp model at depths of 0, 10, 20 and 30 km. Compared to the Qp model shown in Figure 29, there are some obvious changes in some regions where earthquakes are concentrated. For example, at the depth of 10 km, the event cluster around latitude 26^{o}N and longitude 100^{o}E was originally located in a high Qp region (Figure 29), but now it is more closely related to a moderate and low Qp region (Figure 30). For comparison, we also calculated the Qp model using the differential t* values obtained directly from absolute t* values. As we noticed previously that the two sets of differential t* values correlate very well (Figure 11), the Qp models are very similar too (Figures 30 and 31).

For the Qs attenuation tomography, we measured ~8860 absolute S-wave t* values for ~2300 event on 25 stations. The grid setting is the same as for the Qp attenuation tomography. The RMS t* value is 0.0286 and the RMS residual after the inversion is 0.0096, indicating the t* values are successfully fit to about 2/3 of their true values with the resulting Qs model. Figure 32 shows horizontal slices of the Qs model at depths of 0, 10, 20 and 30 km. The high and low Q anomalies are very similar in Qp and Qs models. For example, the high Qs region around latitude 26^{o}N and longitude 100^{o}E also corresponds to a high Qp region. Between the Wuliangshan Fault (F3) and the Red River Fault (F2), there also exists a low Qs anomaly.

We also updated the Qs model using the differential S-wave t* values measured from fitting spectral ratios for two events and two stations (Figure 33) and calculated directly from the absolute S-wave t* values (Figure 34). There are ~122500 differential t* values corresponding to ~1450 events and 24 stations. There are some clear changes in the Qs model using the differential t* values. For example, at the depth of 20 km, in the western side of the study region, the Qs values are uniformly high from the inversion of absolute t* values (Figure 32). However, locally low Qs anomaly zones are imaged around latitude 25^{o}N and longitude 100^{o}E where earthquakes are distributed (Figures 33 and 34). Similar features can be observed in the two Qs models updated using different sets of differential S-wave t* values. Because of strong correlations in differential t* values measured using the two different methods and the similarities in the Q models for both P and S waves, it is therefore reasonable to use the differential t* values calculated directly from the absolute t* values.

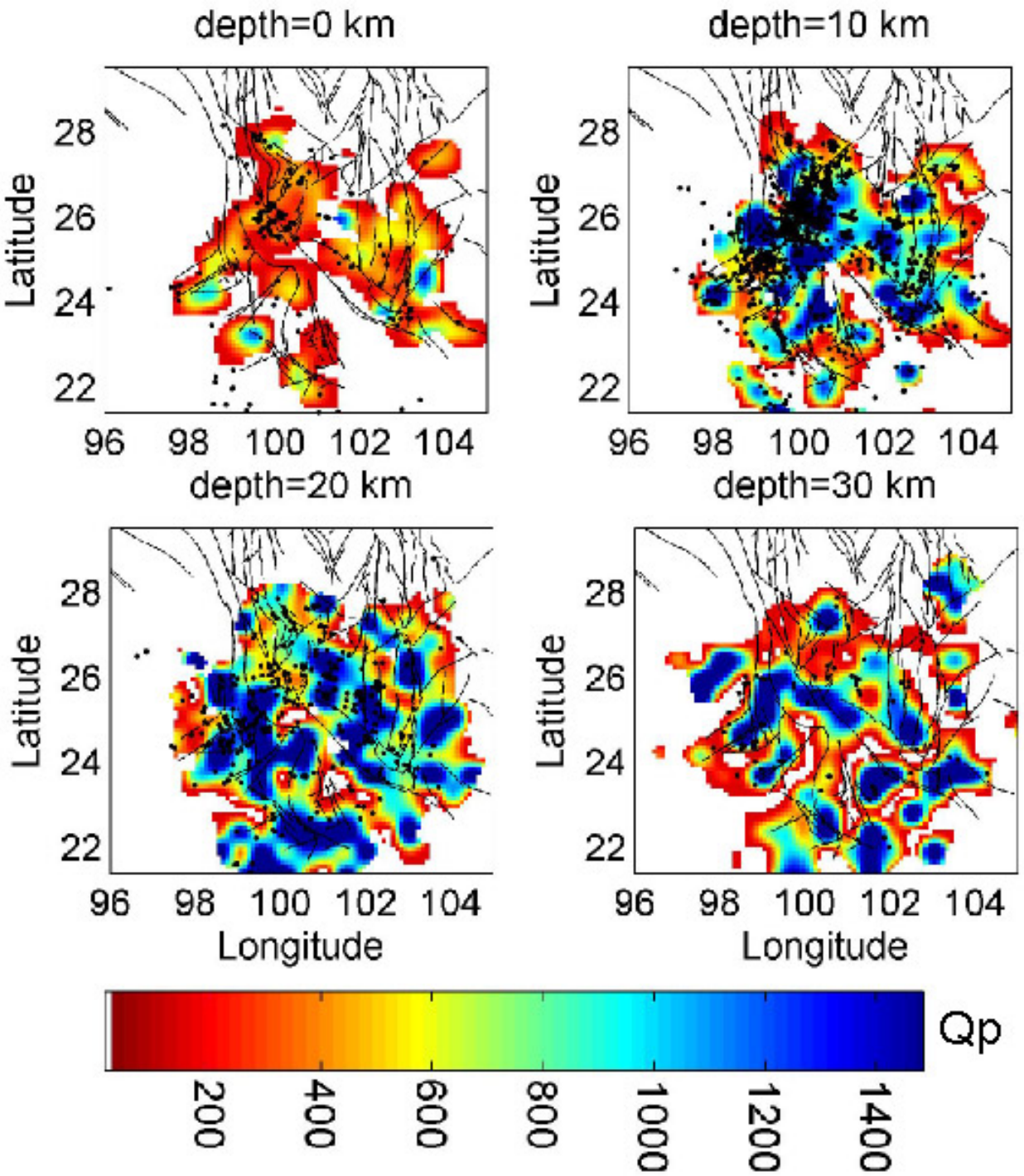

Figure 29. Horizontal slices of the Qp model at depths of 0, 10, 20, and 30 km calculated using the t* values estimated from the omega-square source model.

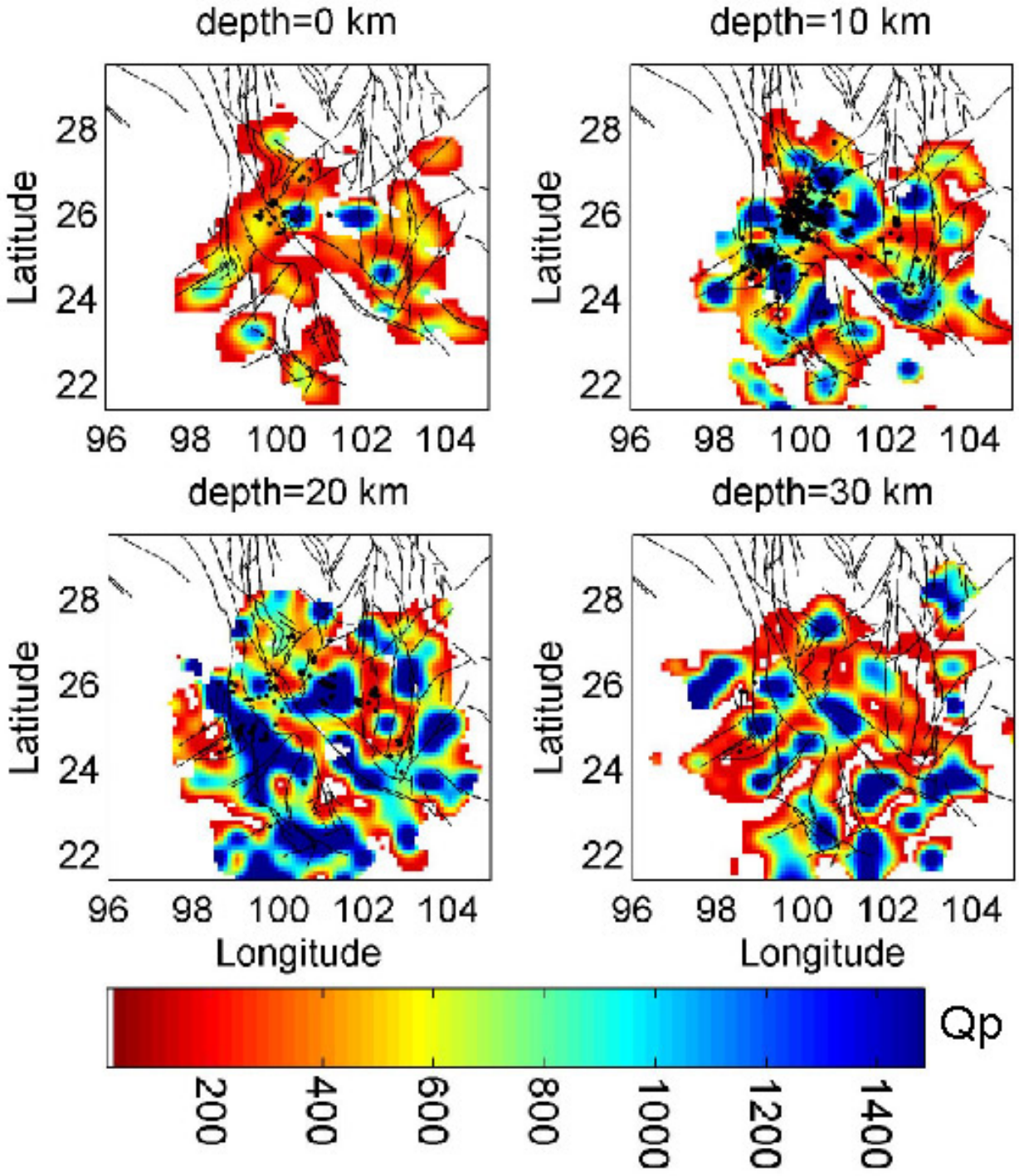

Figure 30. Horizontal slices of the Qp model at depths of 0, 10, 20, and 30 km calculated using the differential t* values estimated from the waveform fitting.

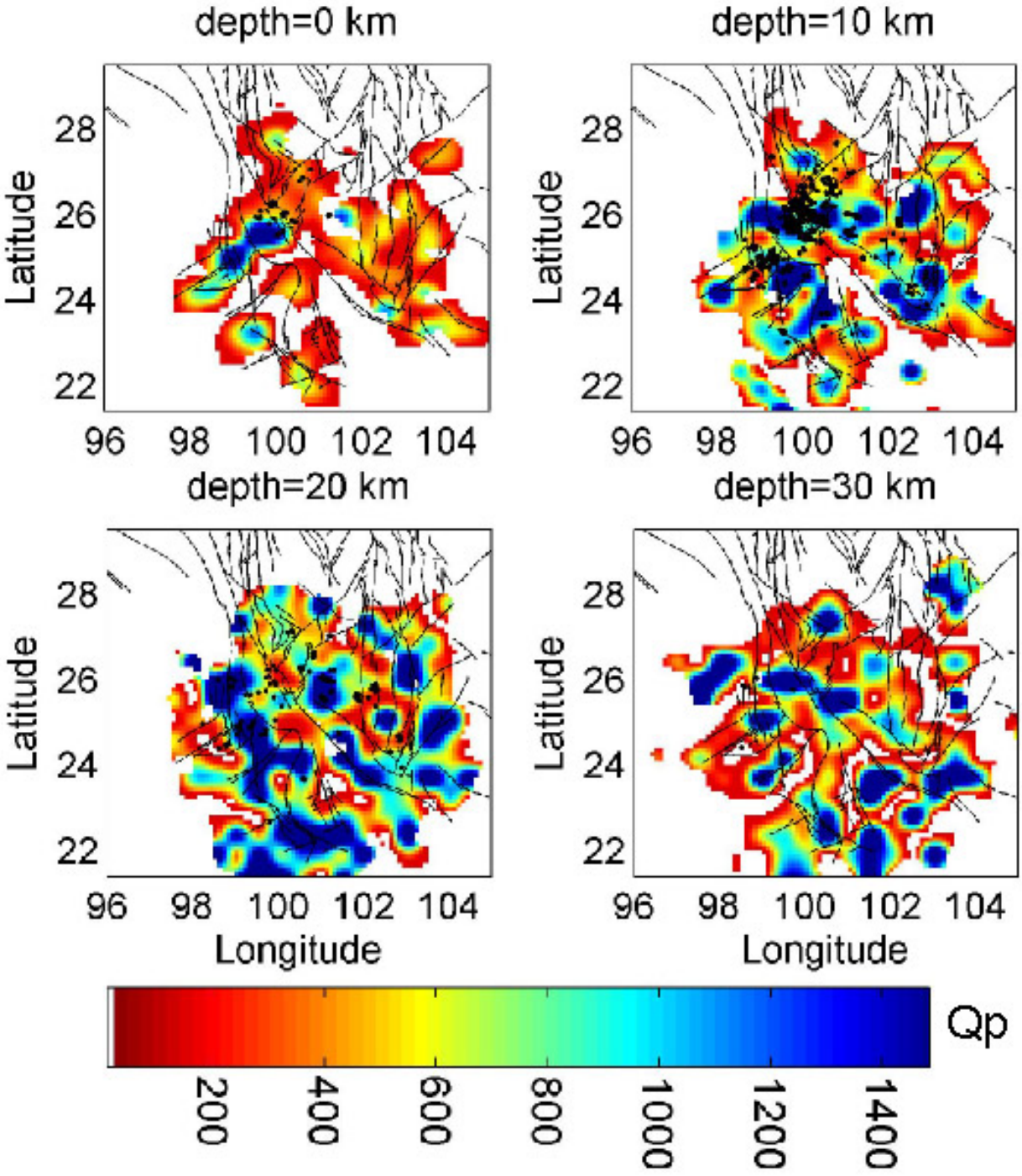

Figure 31. Horizontal slices of the Qp model at depths of 0, 10, 20, and 30 km calculated using the differential t* values estimated directly from absolute t* values.

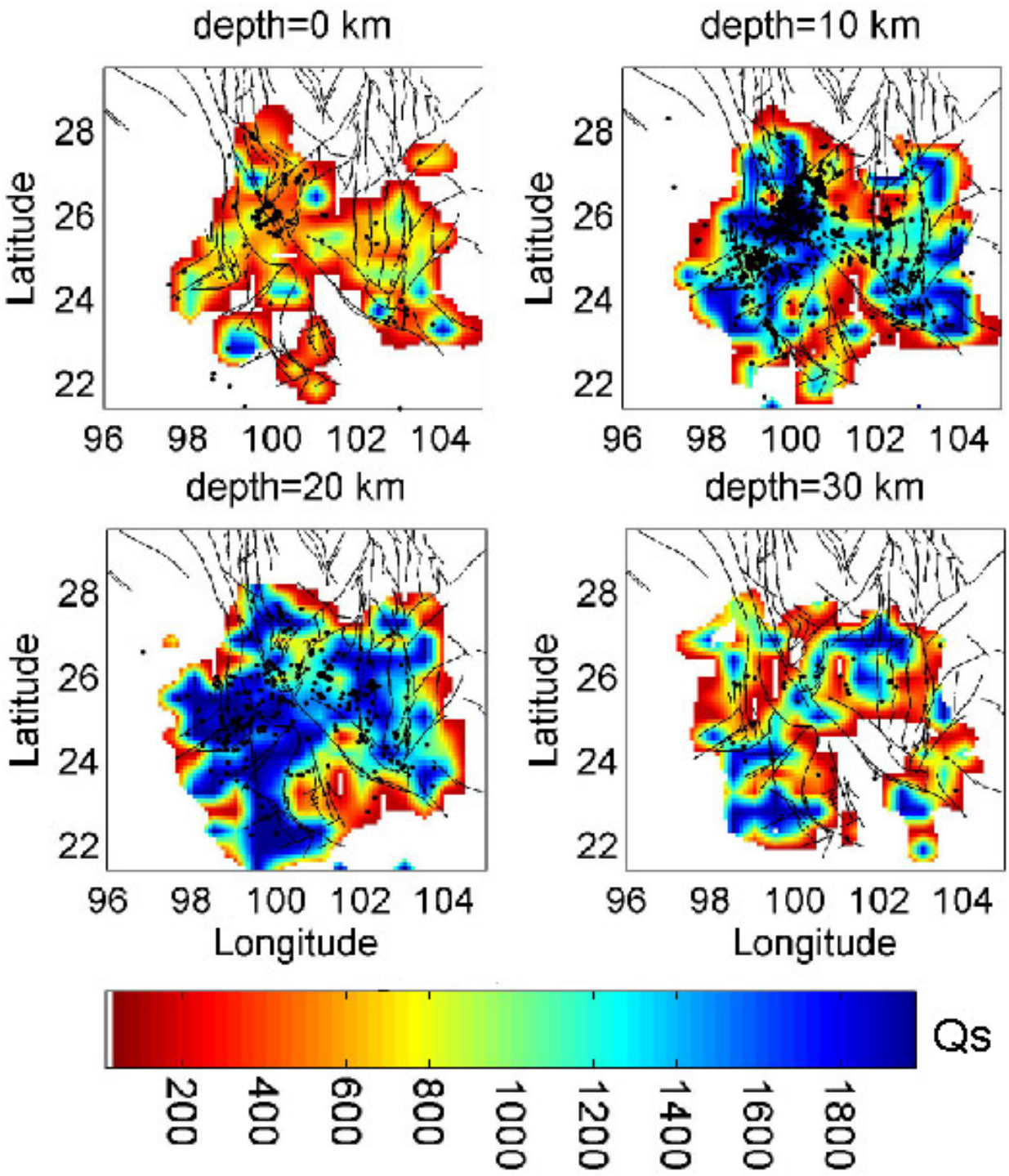

Figure 32. Horizontal slices of the Qs model at depths of 0, 10, 20, and 30 km calculated using the t* values estimated from the omega-square source model.

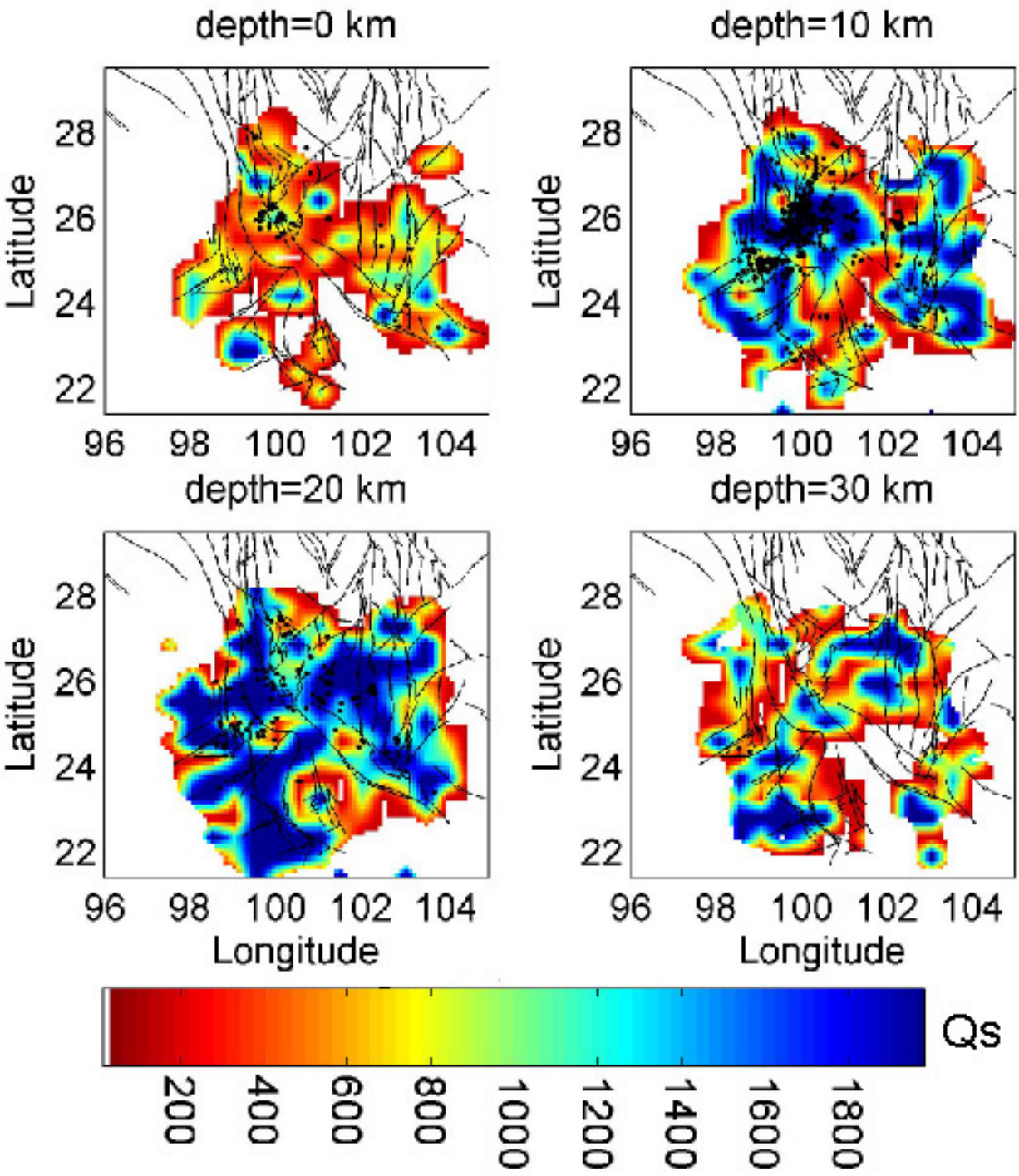

Figure 33. Horizontal slices of the Qs model at depths of 0, 10, 20, and 30 km calculated using the differential t* values estimated from the waveform fitting.

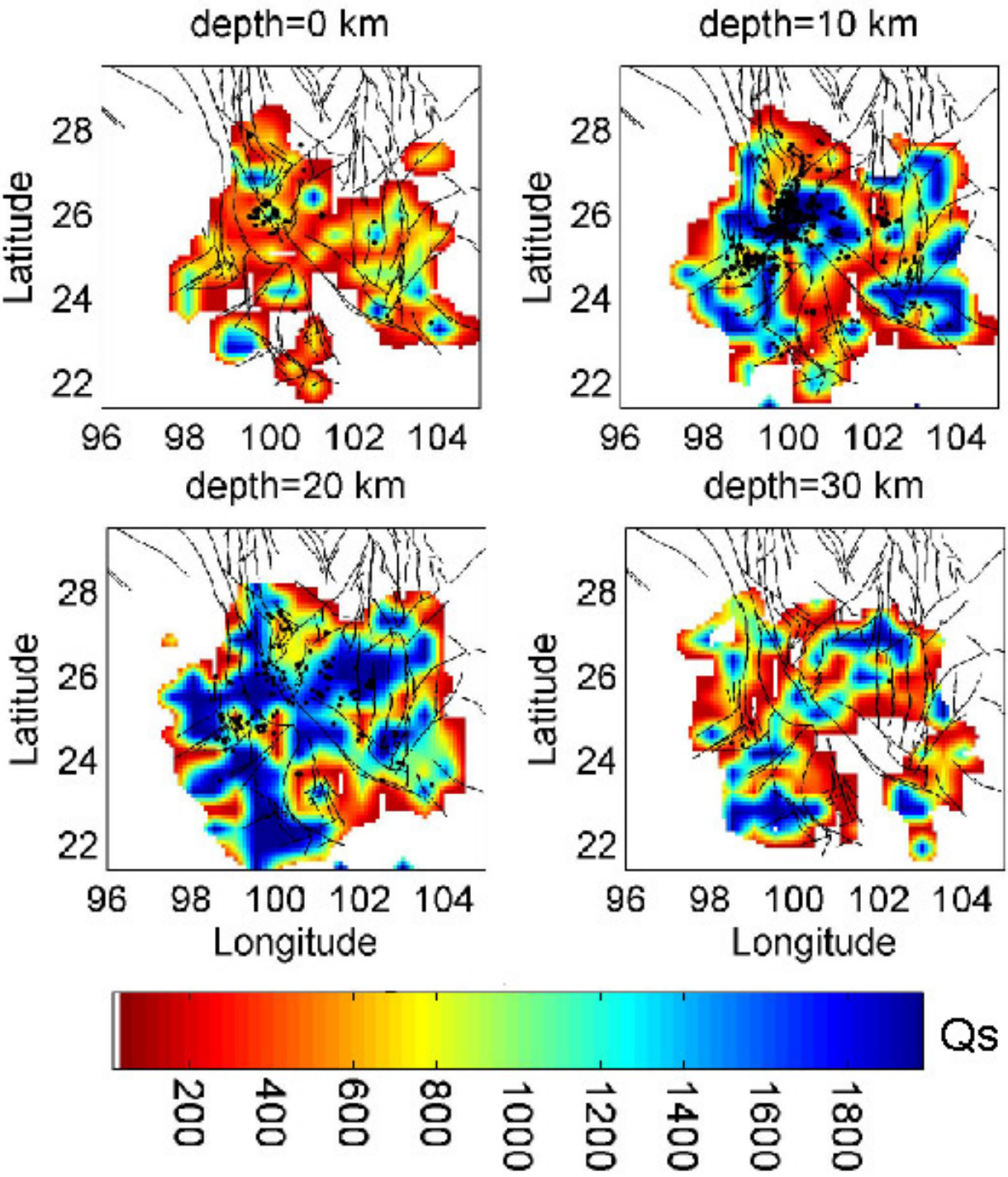

Figure 34. Horizontal slices of the Qs model at depths of 0, 10, 20, and 30 km calculated using the differential t* values estimated directly from the absolute t* values.

9. Assembling ground truth events in the Yunnan region

Determining accurate seismic locations and estimating their uncertainties are of fundamental importance to ground-truth based nuclear explosion monitoring. The traditional ways to determine location uncertainties include the methods based on *a posteriori* residual distribution (Flinn, 1965) or *a priori* uncertainty for phase picking and travel time prediction (Evernden, 1969). Both methods assume that the error processes are Gaussian, zero mean and uncorrelated. In most seismic location practices, these basic statistical assumptions are not satisfied. Thus, the uncertainty in these formal calculations could be underestimated (Myers and Schultz, 2001). An alternative way to assess catalogue location accuracy is based on the station geometry. Using Monte Carlo simulations of network geometry, Bondar et al. (2004) found the local network locations ($0^o - 2.5^o$ epicentral distance) are accurate to within 5 km with a 95 percent confidence level (GT5 $_{95\ percent}$) when the network meets the following criteria: (1) there are at least 10 stations within 250 km; (2) an azimuth gap of less than 110^o; (3) a secondary azimuth gap of less than 160^o; (4) at least one station within 30 km from the event epicenter.

We use similar criteria as defined by Bondar et al. (2004) to classify the earthquakes with magnitude 4 or greater in the Yunnan region from 1999 to 2004. The Yunnan seismic network consists of 26 stations distributed in a 6^ox7^o area. Some stations are just beyond the local epicentral distance of 280 km. Thus, we have to tailor the first two sets of criteria to satisfy our situation. There are a number of events with magnitude 4 or above that meets the first 3 criteria of GT5 $_{95\ percent}$ defined by Bondar et al. (2004). However, only a few of them conform to the 4^{th} criterion. As indicated in Bondar et al. (2004), this constraint is mainly used to ensure that the event is within the crust. As discussed in previous sections, our candidate events are all crustal events with high confidence, thus, we reasonably relax the 4^{th} constraint to that there is at least one station within 100 km of the epicenter. There are a total of 22 earthquakes with magnitude 4 or greater to match the 4 criteria. The average number of stations that record these events is 19 with an average epicentral distance less than 280 km. Taking into account that the accurate 3D velocity model used in relocation, the location accuracy for these earthquakes should be well within 5 km. We ascribe them to the GT5 category. The catalog information for these GT5 reference events is listed in Table 1 and their locations are shown in Figure 35. From Figure 35, we can see that these GT5 reference events are located in the central area of the study region and are surrounded by the network stations.

Table 1. Event information for the assembled GT5 earthquakes.

Year	mon	day	hour	min	sec	lat.	Lon.	depth	Mag
1999	7	17	15	55	47.23	24.7545	99.6991	10.30	4.2
1999	12	7	11	22	42.36	24.6331	102.8813	12.11	4.0
2000	1	15	0	20	15.15	25.5782	101.0424	9.62	4.7
2000	1	15	1	3	43.28	25.5885	101.0179	17.36	4.1
2000	1	23	0	21	19.65	25.5785	101.054	14.04	4.3
2000	6	30	0	27	45.79	25.5847	101.0459	13.26	4.1
2000	8	21	13	25	38.65	25.7424	102.2824	4.84	5.1
2001	3	13	11	42	35.67	25.0082	101.4257	11.20	4.0
2001	4	15	2	11	57.52	24.0376	99.4911	29.42	4.4
2001	5	24	2	23	37.39	24.9524	103.0299	18.92	4.2
2001	9	4	4	5	54.47	23.6743	100.6269	13.22	4.9
2001	9	6	12	13	32.57	26.1814	100.7509	8.21	4.2
2002	5	13	1	52	3.17	25.3018	103.1218	8.71	4.6
2002	7	25	0	34	56.31	25.5838	101.0258	14.85	4.0
2003	7	21	15	16	28.94	25.9857	101.2480	3.22	6.5
2003	8	12	15	59	39.97	26.0222	101.0420	6.70	4.7
2003	8	18	10	0	16.09	25.9577	101.2380	12.79	4.7
2003	9	27	1	6	28.55	25.9644	101.2311	15.59	4.2
2004	2	9	4	30	11.40	25.7581	99.9375	17.77	4.6
2004	5	14	1	54	51.74	25.8603	102.2713	9.44	4.0
2004	6	10	2	14	24.93	25.5386	101.8908	18.22	4.5

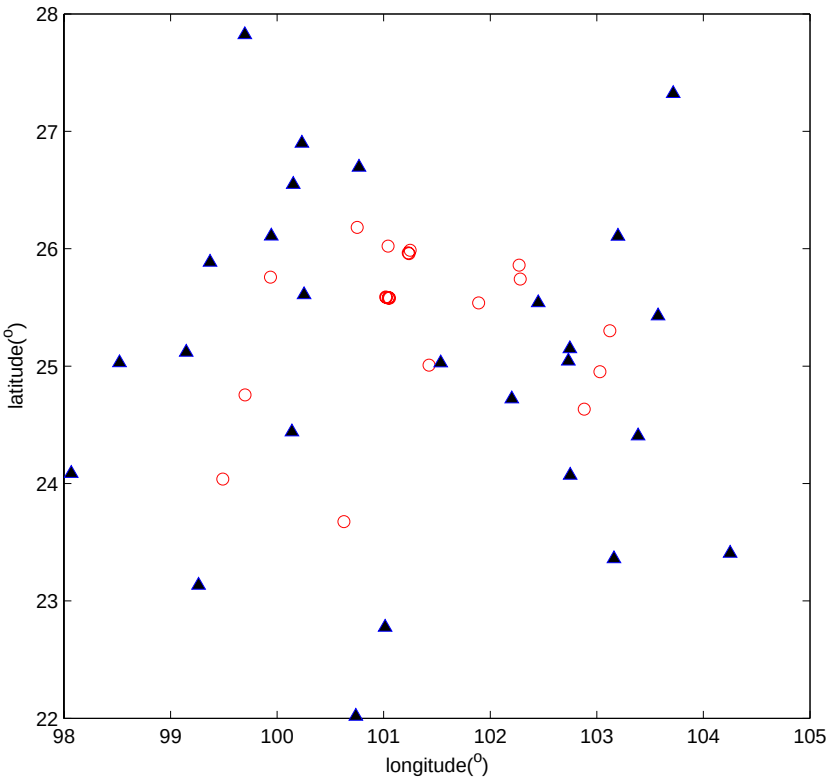

Figure 35. Locations of GT5 reference earthquakes.

10. Conclusions

We have developed an adaptive-mesh "sphere-in-a-box" version of the DD tomography code and applied it to the Yunnan-Sichuan region using catalog P and S picks and waveform CC times (for the Yunnan region). Both P- and S-wave velocity models show strong velocity heterogeneities, consistent with the nature of this active transition zone between the Yangtze platform to the east and the Tibetan plateau to the west. Strong velocity contrasts are evident across some major fault zones and the velocity models are consistent with the regional geology.

The accuracy of event locations is greatly improved compared to catalog locations due to the use of more accurate 3D velocity models and more accurate differential times (waveform CC times and/or catalog differential times). A much sharper image of the seismicity is obtained after relocation for the Yunnan region compared to the diffuse and biased original catalog locations. Many linear features and clusters can be identified in the newly determined event locations. The majority of the events in the Yunnan region are located within the depth range from 5 to 20 km and peak around 12 km. The previous study using the DD location method also found most of the earthquakes in the Yunnan region are shallower than 20 km, but they reported a rather uniform event distribution from 0 to 20 km (Yang et al., 2005). There are more deeper earthquakes down to 40 km in the Sichuan region. Using the modified Bondar criteria to select GT events, we selected 22 earthquakes with magnitude 4 or above to be likely GT5 events.

We also measured absolute and differential P- and S-wave t* values for the Yunnan region. Qp and Qs models are calculated using the absolute and differential t* values using the NNLS algorithm to prevent unphysical negative Q values. Overall, the Qp and Qs models using the absolute t* values show many similar features and are consistent with the velocity models and the local geology. The Qp and Qs models updated using the differential t* values show evident improvement in regions where earthquakes are distributed. We also found that the differential t* values measured using the least squares line fit to the spectral ratios for two events and two stations correlate well with those calculated directly from absolute t* values. Therefore, it is reasonable to use the absolute t* values to directly construct the differential t* values to update the Q models.

11. References

Aki, K., and W. H. K. Lee (1976). Determination of three-dimensional velocity anomalies under a seismic array using first O arrival times from local, earthquakes, I: A homogenous initial model, *J. Geophys. Res.* **81:** 4381-4399.

Barber, C.B., Dobkin, D.P., and Huhdanpaa, H.T. (1996). The Quickhull algorithm for convex hulls, *ACM Trans. on Mathematical Software* **22 (4)**: 469-483.

Beaumont, C., Jamieson, R.A., Nguyen, M.H. & Medvedev, S. (2004). Crustal channel flows: 1. Numerical models with applications to the tectonics of the Himalayan-Tibetan orogen, *J. geophys. Res.,* **109,** B06406, doi:10.1029/2003JB002809.

Blakeslee, S., P. Malin, and M. Alvarez (1989). Fault-zone attenuation of high-frequency seismic waves, *Geophys. Res. Letts.,* **16**: 1321-1324.

Bohm, G., P. Galuppo, and A. Vesnaver (2000). 3D adaptive tomography using Delaunay triangles and Voronoi polygons, *Geophys. Prospect.* **48**: 723-744.

Bondar, I., S.C. Myers, E.R. Engdahl, and E. A. Bergman (2004). Epicentre accuracy based in seismic network criteria, *Geophys. J. Int.,* **56**: 483-496.

Chan, W. W., C. Y. Wang, and W. D. Mooney (2001). 3-D crustal structure in southwestern China, in *Proc. of 23rd Seismic Research Review: Worldwide Monitoring of Nuclear Explosions,* 12-20.

Du, W.X., C.H. Thurber, and D. Eberhart-Phillips (2004). Earthquake relocation using cross-correlation time delay estimates verified with the bispectrum method, *Bull. Seismol. Soc. Am.*, **94**: 856-866.

Eberhart-Phillips, D., W. Stanley, B. Rodriguez, and W. Lutter (1995). Surface seismic and electrical methods to detect fluids related to faulting, *J. Geophys. Res.,* **100**: 12,919-936.

Evernden, J. (1969). Precision of epicenters obtained by small number of world wide stations, *Bull. Seism. Soc. Am.*, **59**: 1365-1398.

Flinn, E. (1965). Confidence regions and error determinations for seismic event location, *Rev. Gephys.*, **3**: 157-185.

Firbas, P. (2000). Location calibration based on 3-D modeling, in *Advances in Seismic Event Location,* C. Thurber and N. Rabinowitz (*eds*), Kluwer, Amsterdam, pp.135-161.

Flanagan, M.P., S.C. Myers, and K.D. Koper (2007). Regional travel-time uncertainty and seismic location improvement using a three-dimensional *a priori* velocity model, *Bull. Seism. Soc. Am.*, **97**: 804 – 825.

He, Z.Q., T.L. Ye, and W. Su (2005). 3-D velocity structure of the middle and upper crust in the Yunnan region, China, *Pure Appl. Geophys.*, **162**: 2355-2368.

Hearn, T. M., and J. F. Ni (2001). Tomography and location problems in China using regional travel-time data, in *Proc. of the 23rd Seismic Research Review: Worldwide Monitoring of Nuclear Explosions,* 277-286.

Hu, H.X., H.X. Lu, and C.Y. Wang (1986). Explosion investigation of the crust structure in western Yunnan Province (in Chinese), *Acta Geophysica. Sinica*, **29**(2): 144-154.

Huang, J.L., X.D. Song, S.Y. Wang (2003). Fine structure of Pn velocity beneath Sichuan-Yunnan region, *Sci. China,* Ser. D, **46** Suppl.: 201-209.

Huang, J., D. Zhao, and S. Zheng (2002). Lithospheric structure and its relationship to seismic and volcanic activity in southwest China, *J. Geophys. Res.*, **107**(B10), 2255, doi:10.1029/2000JB000137.

Jiao, W., W. Chan, R. Herrmann, and R.A. Wagner (2003). Discrimination studies in the Yunnan region, southwest China, in *25th Seismic research Review – Nuclear Explosion Monitoring: Building the Knowledge Base*, 405-419.

Kissling, E., F. Haslinger, and S. Husen (2001). Model parametrization in seismic tomography: A choice of consequence for the solution quality, Phys. Earth Plan. Int., 123: 89-101.
Lawson, C.L., and R.J. Hanson (1974). Solving least squares problems, Prentice-Hall, Englewood Cliffs, N.J., 340 pp., 1974.
Laske, G., G. Masters, and C. Reif (2001). Crust 2.0: a new global crustal model at 2×2 degrees, http://mahi.ucsd.edu/Gabi/rem.dir/crust/crust2.html.
Lebedev, S., and G. Nolet (2003). Upper mantle beneath southeast Asia from *S* velocity tomography, *J. Geophys. Res.* **108**, no. B1, 2048, doi 10.1029/2000JB000073.
Lees, J. M., and G.T. Lindley (1994). Three-dimensional attenuation tomography at Loma Prietal inversion of t* for Q, *J. Geophys. Res.,* **99**: 6843-6836.
Li, C., Van der Hilst, R.D. & Toksoz, M.N. (2006). Constraining P-wave velocity variations in upper mantle beneath Southeast Aisa, *Phys. Earth Planet. Inter.,* **154**: 180–195.
Li, P. (1993). The Xiansuihe-Xiaojiang Fault Zone, Seismological Press, Bejing, 267 pp. (in Chinese).
Liang, C.T., X.D. Song, J.L. Huang (2004). Tomographic inversion of Pn travel-times in China, *J. Geophys. Res.,* 109, B11304, doi:10.1029/2003JB002789.
Lin, Z.Y., H.X. Hu, and W.B. Zhang (1993). The preliminary interpretation of deep seismic sounding in western Yunnan, *Acta Seismol. Sinica*, **6**(4): 867-881.
Liu, Y., X. Chang, J. He, F. Liu, and H. Sun (2005).Three-dimensional velocity images of the crust and upper mantle beneath the North-South Zone in China, *Bull. Seism. Soc. Am.*, **95**(3): 916-925.
Liu, F. T., H. Wu, J. H. Liu, G. Hu, Q. Li, and K.X. Qu (1990), 3-D velocity images beneath the Chinese continent and adjacent regions, *Geophys. J. Int.,* **101**: 379-394.
Michelini, A., and T. V. McEvilly (1991). Seismological studies at Parkfield. I. Simultaneous inversion for velocity structure and hypocenters using cubic B-splines parameterization, *Bull. Seism. Soc. Am.* **81**: 524-552.
Mooney, W. D. (1998). Crust 5.1: a global crustal model at $5^{o}\times5^{o}$, *J. Geophys. Res.,* **103**: 727-747.
Myers, S.C., and Shultz, C.A. (2001). Statistical characterization of reference event accuracy, *Seism. Res. Lett.*, **72**: 244.
Nikias, C.L., and R. Pan (1988). Time delay estimation in unknown Gaussian spatially correlated noise, *IEEE Trans. Acoust. Speech Signal Process,* **36**: 1706.
Nikias, C.L., and M.R. Raghuveer (1987). Bispectrum estimation: A digital signal processing framework, *Proc. IEEE*, **75**: 869.
Park, J., C.R. Lindberg, F.L. Vernon (1987). Multitaper spectral-analysis of high-frequency seismograms, *J. Geophys. Res.*, **92** (B12): 12675-12684.
Podvin, P., and I. Lecomte (1991). Finite difference computation of travel times in very contrasted velocity models: a massively parallel approach and its associated tools, *Geophys. J. Int.* **105**: 271-284.
Ren, J. S., C. F. Jiang, and Z. K. Zhang (1980).Tectonics in China and Its Evolution (in Chinese), 124 pp., Science Press, Beijing.
Rietbrock, A. (2001). P wave attenuation structure in the fault area of the 1995 Kobe earthquake, *J. Geophys. Res.,* **106**: 4141-4151.

Ritzwoller, M..H., M. P. Barmin, A. Villasenor, A. L. Levshin, and E. R. Engdahl (2002). Pn and Sn tomography across Eurasia to improve regional seismic event locations, *Tectonophysics*, **358:** no.1-4, 39-55.

Romero, A. E., T.V. McEvilly, and E.L. Majer (1997). 3-D microearthquake attenuation tomography at the Northwest Geysers geothermal region, California, *Geophys.,* **62:** 149-167.

Roth, E.G., and D.A. Wiens (1999). Seismic attenuation tomography of the Tonga-Fiji region using phase pair methods, *J. Geophys. Res.,* **104**: 4795-4809.

Royden, L.H., Burchfiel, B.C., King, R.W., Wang, E., Chen, Z., Shen, F. & Yuping, L. (1997). Surface deformation and lower crustal flow in eastern Tibet, *Science,* **276**: 788–790.

Sambridge, M., Braun, J., and McQueen, H. (1995). Geophysical parametrization and interpolation of irregular data using natural neighbours, *Geophys. J. Int.,* **122**: 837-857.

Sambridge, M., and O. Gudmundsson (1998). Tomographic systems of equations with irregular cells, *J. Geophys. Res.,* **103**: 773-781.

Sambridge, M., and R. Faletic (2003). Adaptive whole Earth tomography, *Geochem. Geophys. Geosyst.,* **4**(3), 1022, doi:10.1029/2001GC000213.

Sanders, C. O. (1993). Local earthquake tomography: attenuation – theory and results, in "Seismic tomography," H. M. Iyer and K. Hirahara (eds.), Chapman and Hall, pp. 676-694

Schaff, D.P., G.H.R. Bokelmann, G.C. Beroza, F. Waldhauser, and W.L. Ellsworth (2002). High-resolution image of Calaveras Fault seismicity, *J. Geophys. Res.*, **107**, 2186, doi:10.1029/2001JB000633.

Shapiro, N. M., and M. H. Ritzwoller (2002). Monto Carlo inversion for a global shear velocity model of the crust and upper mantle, *Geophys. J. Int.,* **151**: 88-105.

Smith, G. P., and G. Ekstrom (1996). Improving teleseismic earthquake locations using a three-dimensional Earth model, *Bull. Seismol. Soc. Am.,* **86**: 123-132.

Steck, L. K., C. R. Bradley, and L. E. Jones (2000). Improved velocity models in western China for two- and three-dimensional finite difference modeling, in *Proc. of the 22nd Seismic Research Review: Planning for verification of and compliance with the comprehensive Nuclear-test-Ban Treaty (CTBT),* New Orleans, September 13-15.

Su, Y.J., and J.Z. Qin (2001). Strong earthquake activity and relation to regional neo-tectonic movement in Sichuan-Yunnan region, *Earthq. Res. China*, **17**(1): 24-34 (in Chinese with English abstract).

Sun, Y., X. Liu, S. Kuleli, D. F. Morgan, and N. M. Toksoz (2004). Adaptive moving window method for 3D P-velocity tomography and its application in China, *Bullet. Seismol. Soc. Am.,* **94**: 740-746.

Teng, J. (1987). Panzhihua-Xichang ancient rift and ''activized'' geophysical features (in Chinese), *Acta Geophys. Sin.*, **30**: 581–593.

Thurber, C.H. (1983). Earthquake locations and three-dimensional crustal structure in the Coyote Lake area, central California, *J. Geophys. Res.*, **88**: 8226-8236.

Thurber, C., and D. Eberhart-Phillips (1999). Local earthquake tomography with flexible gridding, *Comp. & Geosci.*, **25**: 809-818.

Thurber, C., S. Roecker, H. Zhang, S. Baher, and W. Ellsworth (2004). Fine-scale structure of the San Andreas fault and location of the SAFOD target earthquakes, *Geophys. Res. Lett.*, ***31,*** doi:10.1029/2003GL019398.

Um, J., and C.H. Thurber (1987). A fast algorithm for two-point seismic ray tracing, *Bull. Seism. Soc. Am.,* **77**: 972-986.

Vesnaver, A. (1996). Irregular grids in seismic tomography and minimum-time ray tracing, *Geophys. J. Int.* **126**: 147-165.

Waldhauser, F. and W.L. Ellsworth (2000). A double-difference earthquake location algorithm: Method and application to the northern Hayward fault, CA, *Bull. Seismol. Soc. Am.,* **90,** 1353-1368.

Wang, C.-Y., W.W. Chan, and W.D. Mooney (2003). Three-dimensional velocity structure of crust and upper mantle in southwestern China and its tectonic implications, *J. Geophys. Res.*, **108**(B9), 2442, doi: 10.1029/2002JB001973, 2003.

Wu, F. T., A. L. Levshin, and V. M. Kozhevnikov (1997). Rayleigh wave group velocity tomography of Siberia, China, and vicinity, *Pure Appl. Geophys.*, **149**: 447–473.

Xie, J., R. Gok, J. Ni, and Y. Aoki (2002). Lateral Variations of Lg Q in the Tibetan Plateau, in *Proc. of 24th Seismic Research Review – Nuclear Explosion Monitoring: Innovation and Integration,* 219-228.

Xie, J. (2003). Pn Q under Tibet and Tienshan with practical and scientific implications, in *Proc. of 25th Seismic Research Review – Nuclear Monitoring: Building the knowledge Base,* 182-190.

Xu, X., W. Li, and Q. Yang (1985). Features and origins of Kangding complex, in Studies of the Continental Rift System in Panzhihua Region (in Chinese), vol. 1, pp. 27– 31, Geol. Press, Beijing.

Xu, Y., F. Liu, J. Liu, and H. Chen (2002). Crust and upper mantle structure beneath western China from P wave travel time tomography, *J. Geophys. Res.,* 107, 2220, doi 10.1029/2001JB000402.

Yang, Z.X., F. Waldhauser, Y.T. Chen & P.G. Richards (2005). Double-difference relocation of earthquake in central-western China, 1992-1999, Journal of Seismology, **9**: 241-264.

Yang, Z., Y. Chen, Y. Zheng, and X. Yu (2003). Accurate relocation of earthquakes in central-western China using the double-difference earthquake location algorithm, Science in China (Series D), *Sci. China,* Ser. D, **46**:, 129-134.

Yao, H., Van der Hilst, R.D., and De Hoop, M.V. (2006). Surface-wave array tomography in SE Tibet from ambient seismic noise and two-station analysis: I - Phase velocity maps, *Geophy. J. Int.*, **166**: 732-744, doi: 10.1111/j.1365-246X.2006.03028.x.

Zhang, H., and C.H. Thurber (2003). Double-difference tomography: method and application to the Hayward fault, California, *Bull. Seismol. Soc. Am.*, **93**: 1875-1889.

Zhang, H., and C. Thurber (2005). Adaptive-grid seismic tomography based on tetrahedral and Voronoi diagrams: Application to Parkfield, California, *J. Geophys. Res*, **110,** B04303, doi:10.1029/2004JB003186.

Zhang, H., and C. Thurber (2006). Development and applications of double-difference tomography, *Pure and Applied Geophys.,* **163**: 373-403, doi:10.1007/s00024-005-0021-y.

Zhang, H., C. H. Thurber, C. A. Rowe (2003). Automatic first-arrival detection and picking with multiscale wavelet analysis, *Bull. Seism. Soc. Am.,* **93**: 1904-1912.

Zhang, H., C. Thurber, D. Shelly, S. Ide, G. Beroza, and A. Hasegawa (2004). High-resolution subducting slab structure beneath Northern Honshu, Japan, revealed by double-difference tomography, *Geology*, **32**: 361-364.

Zhao, D., F. Ochi, A. Hasegawa, and A. Yamamoto (2000). Evidence for the location and cause of large crustal earthquakes in Japan, *J. Geophys. Res.*, **105**: 13579-13594.